A&A 645, A49 (2021)
https://doi.org/10.1051/0004-6361/202039047

Astronomy & Astrophysics

A proto-pseudobulge in ESO 320-G030 fed by a massive molecular inflow driven by a nuclear bar

Eduardo González-Alfonso[1,2], Miguel Pereira-Santaella[3], Jacqueline Fischer[4], Santiago García-Burillo[5], Chentao Yang (杨辰涛)[6], Almudena Alonso-Herrero[7], Luis Colina[3], Matthew L. N. Ashby[2], Howard A. Smith[2], Fernando Rico-Villas[3], Jesús Martín-Pintado[3], Sara Cazzoli[8], and Kenneth P. Stewart[4]

[1] Universidad de Alcalá, Departamento de Física y Matemáticas, Campus Universitario, 28871 Alcalá de Henares, Madrid, Spain
e-mail: eduardo.gonzalez@uah.es
[2] Center for Astrophysics Harvard & Smithsonian, 60 Garden Street, Cambridge, MA 02138, USA
[3] Centro de Astrobiología (CSIC-INTA), Ctra. de Ajalvir, km. 4, 28850 Torrejón de Ardoz, Madrid, Spain
[4] George Mason University, Department of Physics & Astronomy, MS 3F3, 4400 University Drive, Fairfax, VA 22030, USA
[5] Observatorio Astronómico Nacional (OAN-IGN)-Observatorio de Madrid, Alfonso XII, 3, 28014 Madrid, Spain
[6] European Southern Observatory, Alonso de Córdova 3107, Casilla 19001, Vitacura, Santiago, Chile
[7] Centro de Astrobiología (CAB, CSIC-INTA), ESAC Campus, 28692 Villanueva de la Cañada, Madrid, Spain
[8] IAA – Instituto de Astrofísica de Andalucía (CSIC), Apdo. 3004, 18008 Granada, Spain

Received 28 July 2020 / Accepted 27 October 2020

ABSTRACT

Galaxies with nuclear bars are believed to efficiently drive gas inward, generating a nuclear starburst and possibly an active galactic nucleus. We confirm this scenario for the isolated, double-barred, luminous infrared galaxy ESO 320-G030 based on an analysis of *Herschel* and ALMA spectroscopic observations. *Herschel*/PACS and SPIRE observations of ESO 320-G030 show absorption or emission in 18 lines of H_2O, which we combine with the ALMA H_2O 4_{23}–3_{30} 448 GHz line (E_{upper} ~ 400 K) and continuum images to study the physical properties of the nuclear region. Radiative transfer models indicate that three nuclear components are required to account for the multi-transition H_2O and continuum data. An envelope, with radius R ~ 130–150 pc, dust temperature $T_{dust} \approx 50$ K, and $N_{H2} \sim 2 \times 10^{23}$ cm^{-2}, surrounds a nuclear disk with R ~ 40 pc that is optically thick in the far-infrared ($\tau_{100\,\mu m}$ ~ 1.5–3, $N_{H2} \sim 2 \times 10^{24}$ cm^{-2}). In addition, an extremely compact (R ~ 12 pc), warm (≈100 K), and buried ($\tau_{100\,\mu m} > 5$, $N_{H2} \gtrsim 5 \times 10^{24}$ cm^{-2}) core component is required to account for the very high-lying H_2O absorption lines. The three nuclear components account for 70% of the galaxy luminosity (SFR ~ 16–18 $M_\odot$ yr^{-1}). The nucleus is fed by a molecular inflow observed in CO 2-1 with ALMA, which is associated with the nuclear bar. With decreasing radius (r = 450–225 pc), the mass inflow rate increases up to $\dot{M}_{inf}$ ~ 20 $M_\odot$ yr^{-1}, which is similar to the nuclear star formation rate (SFR), indicating that the starburst is sustained by the inflow. At lower r, ~100–150 pc, the inflow is best probed by the far-infrared OH ground-state doublets, with an estimated $\dot{M}_{inf} \sim 30\,M_\odot$ yr^{-1}. The inferred short timescale of ~20 Myr for nuclear gas replenishment indicates quick secular evolution, and indicates that we are witnessing an intermediate stage (<100 Myr) proto-pseudobulge fed by a massive inflow that is driven by a strong nuclear bar. We also apply the H_2O model to the *Herschel* far-infrared spectroscopic observations of $H_2^{18}O$, OH, ^{18}OH, OH^+, H_2O^+, H_3O^+, NH, NH_2, NH_3, CH, CH^+, $^{13}CH^+$, HF, SH, and C_3, and we estimate their abundances.

Key words. galaxies: bulges – galaxies: clusters: individual: ESO 320-G030 – galaxies: evolution – galaxies: nuclei – infrared: galaxies – submillimeter: galaxies

1. Introduction

The funneling of large amounts of gas into galaxies' nuclear regions has profound consequences for galaxy evolution because it triggers starbursts and leads to buried galactic nuclei that are characterized by high column densities and dust temperatures. This is followed by a rapid growth of supermassive black holes (SMBHs), which appear to gain most of their mass in bright quasar modes (Soltan 1982). Eventually, feedback unbinds the local gas supply, terminating the inflow and stalling further SMBH growth (e.g., Younger et al. 2008). While mergers are one obvious mechanism for generating central mass concentrations, secular evolution via mass inflows caused by disk instabilities such as bars can generate pseudobulges (Kormendy 1982; Kormendy & Kennicutt 2004; Combes & Sanders 1981); however, the physical properties of such nuclei while they are still assembling gas are not always well understood because of the high obscuration.

Taking advantage of the availability of far-infrared (far-IR) and (sub)millimeter (submm) wavelengths facilities is the best way to overcome these difficulties. Spectroscopy of buried nuclei in the far-IR with the Infrared Space Observatory and the *Herschel* Space Observatory has revealed high excitation of light hydrides, mostly water vapor (H_2O) and hydroxyl (OH), with the far-IR (<200 μm) lines detected in absorption and lines at longer wavelengths observed in emission (e.g., González-Alfonso et al. 2004, 2008, 2012, 2017, and references therein). The specific characteristic of these lines, as compared with the rotational lines of other more commonly used tracers (CO, HCN, HCO^+, etc), is that their rotational levels are excited through the intense far-IR radiation generated in buried galactic nuclei, thus directly probing the generation of the bulk of the luminosity in these

environments. The line ratios are thus sensitive to the strength of the far-IR radiation density responsible for the excitation, and the absolute line fluxes constrain the effective sizes of the involved regions, which will be similar to the physical sizes when the surface filling factor is ∼1. This provides an effective spatial resolution that is much better than the low spatial resolution of these powerful spectroscopic observations. These nuclei are also directly imaged through observations of the continuum at (sub)mm wavelengths (e.g., Sakamoto et al. 2013) or through the observation of vibrationally excited lines of HCN (e.g., Aalto et al. 2015) and HC_3N (e.g., Rico-Villas et al. 2020). Nevertheless, it is highly desirable to combine these far-IR observations of H_2O with (sub)mm interferometric observations of a transition of the same species, providing a more direct and complementary way to probe the size and morphology of highly obscured nuclear regions.

With ALMA, the first detections in space of the ortho-H_2O $4_{23} - 3_{30}$ transition at 448 GHz (H_2O448), both in the local Universe (Pereira-Santaella et al. 2017) and at high redshift (Yang et al. 2020), offer a new way to address the need to spatially resolve these regions. Despite the large difference in the infrared luminosities of the two reported detections in H_2O448 ($L_{IR} = 1.7 \times 10^{11}\,L_\odot$ for the local luminous infrared galaxy (LIRG) ESO 320-G030, also identified as IRAS 11 506-3851, and $\sim 10^{13}\,L_\odot$ for the $z = 3.6$ merger G09v1.97), the fractional luminosity of the H_2O448 line is similar ($L_{H_2O448}/L_{IR} \approx (0.85\text{–}2) \times 10^{-7}$); this is surprising because in both sources the line is generated in a small nuclear region that accounts for only a fraction of the total galaxy luminosity.

The main characteristics that make this line a unique probe of buried stages of galactic nuclei are (see also Pereira-Santaella et al. 2017; Yang et al. 2020): (i) Owing to the long wavelength of the line and low transition probabilities, it is a deeper probe than other H_2O lines at shorter wavelengths. (ii) The high energy of the involved rotational levels (>400 K) guarantees the filtering out of relatively cold extended regions, thus specifically tracing the warmest nuclear regions. The line in ESO 320-G030 indeed comes from a region that is even more compact than the continuum emission at 448 GHz, but it is spatially resolved with ALMA clearly probing the innermost rotating disk. (iii) Radiative transfer calculations confirm that the H_2O448 line is pumped through absorption of far-IR photons in the high-lying H_2O lines at 79 and 132 μm, and the 79 μm line (4_{23}–3_{12}) is indeed observed in absorption with *Herschel* toward buried galactic nuclei including ESO 320-G030, thus tracing the far-IR absorption detected with *Herschel*/PACS. (iv) While the H_2O448 line is strong, our models indicate that it is not a maser (which would be difficult to interpret due to the uncertain amplification), and the low A-Einstein coefficient ensures that the transition requires high columns to emit at the observed level. (v) The H_2O448 line can be modeled, in combination with other H_2O lines at shorter wavelengths, to provide crucial parameters such as the nuclear IR luminosity, the columns of gas, the continuum opacities, dust temperatures, and the kinematics of the warm and luminous nuclear ISM.

The observation of multiple H_2O lines is required to obtain a complete description of buried nuclear regions, which can be thought of as an ensemble of components with differing characteristics. The most extreme nuclear components, characterized by optical depths at 100 μm $\tau_{100} \gg 1$ and dust temperatures $T_{dust} \gtrsim 100$ K, are best identified with far-IR absorption lines with level energies at ≳600 K (González-Alfonso et al. 2012). On the other hand, the opaque nuclei are surrounded by massive ISM components with moderate column densities and T_{dust}, which are best traced by the H_2O lines at 240–400 μm lines with level energies below ≈300 K. Pereira-Santaella et al. (2017) presented a model of the nucleus of ESO 320-G030 based on the H_2O448 ALMA emission line and the pumping H_2O 79 μm *Herschel* absorption line. While the analysis of these two lines alone provided the average properties of a starburst nuclear disk in the galaxy, the extremely rich spectrum of H_2O in the far-IR and submm allows us to obtain a more complete description of the nuclear region. As shown below, up to 18 lines of H_2O have been detected with *Herschel* in ESO 320-G030. In this paper, we fully exploit the *Heschel*/ALMA synergy with the goal of inferring the physical conditions in the nuclear region of ESO 320-G030 from the full set of H_2O absorption and emission lines.

At a distance of 48 Mpc (233 pc arcsec^{-1}, Pereira-Santaella et al. 2017), ESO 320-G030 is morphologically classified as class 0 (i.e., an isolated galaxy with a symmetric disk and no sign of past or ongoing interaction; Arribas et al. 2008), and with a regular velocity rotational field (Bellocchi et al. 2013, 2016). Nevertheless, it is a double-bar system (Greusard et al. 2000), with the nuclear bar (PA = 75°, radius of ∼0.8 kpc) nearly perpendicular to the primary bar (∼9 kpc, Pereira-Santaella et al. 2016). Evidence of high nuclear star formation activity and obscuration has already been derived from optical and near-IR observations (Alonso-Herrero et al. 2006; Rodríguez-Zaurín et al. 2011; Piqueras López et al. 2016), and the relatively deep 9.7 μm silicate absorption (Pereira-Santaella et al. 2010a). While far-IR spectroscopy shows inverse P-Cygni profiles in the ground-state OH doublets suggesting inflowing gas (Fig. 11 in González-Alfonso et al. 2017, and Sect. 4.2 below), outflows from the nucleus have also been detected in Hα (Arribas et al. 2014) and NaD (Cazzoli et al. 2014, 2016) with moderate velocities (≲100 km s^{-1}), and in CO 2-1 with higher velocities (Pereira-Santaella et al. 2016, 2020). There is no clear evidence for the presence of an active galactic nucleus (AGN), either from mid-IR indicators such as the undetected [O IV] and [Ne V] tracers or the mid-IR slope of the continuum (Pereira-Santaella et al. 2010b; Alonso-Herrero et al. 2012), the observed radio properties (in a survey of OH megamaser galaxies by Baan & Klöckner 2006), or from the X-ray emission and the optical spectral classification (Pereira-Santaella et al. 2011). ESO 320-G030 can be thus considered a prototype of an isolated galaxy with strong secular evolution driven by bars during a phase of central gas assembly with feedback already in action.

This paper is structured as follows. We present the observations in Sect. 2; the analysis of the H_2O data and the continuum, including a 3D modeling approach, is described in Sect. 3; we discuss the formation of the buried nucleus in ESO 320-G030 in light of the CO 2–1 ALMA observations at higher spatial scales in Sect. 4, including an estimate of the mass inflow rate based on the CO data cube and on the far-IR profiles of the OH doublets. Our findings are discussed and summarized in Sect. 5. We also present in Appendix A all *Herschel*/PACS wavelength ranges observed in ESO 320-G030, and apply the H_2O-based model to all other observed absorption molecular features to estimate the molecular abundances.

2. Observations

2.1. Herschel /PACS data

The *Herschel*/PACS (Pilbratt et al. 2010; Poglitsch et al. 2010) spectra presented here were obtained as part of the *Herschel* Open Time (OT2) program HerMoLirg (PI: E. González-Alfonso), which aimed to observe a set of molecular

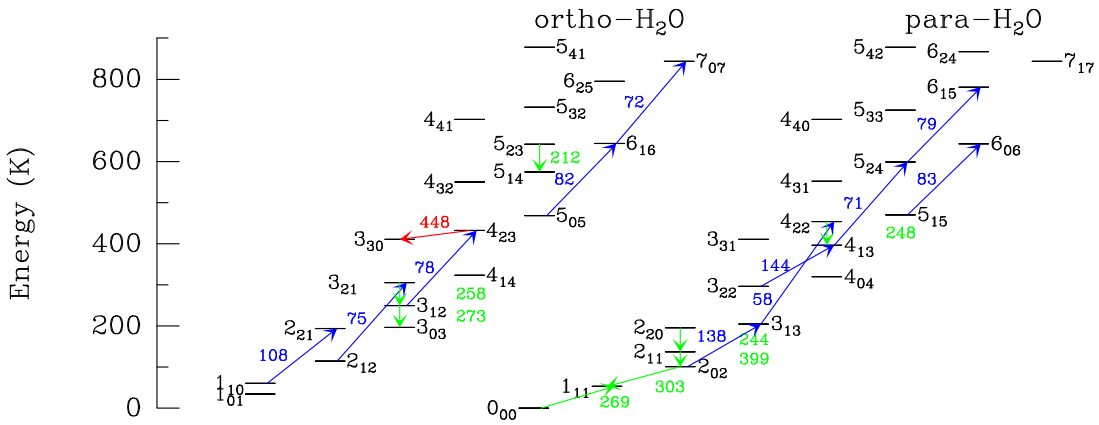

Fig. 1. Energy level diagram of H_2O indicating the lines observed with *Herschel*/PACS (blue arrows and labels), with *Herschel*/SPIRE (green), and with ALMA (red). Labels denote the rounded wavelengths in μm as indicated in the second column of Table 1, except for the line observed with ALMA which is denoted by its frequency in GHz. Upward (downward) arrows indicate lines detected in absorption (emission).

lines including H_2O in a sample of local (Ultra-)Luminous Infrared Galaxies ((U)LIRGs). The observed lines are indicated with blue arrows in the energy level diagram of Fig. 1. The spectra were observed in high spectral sampling range-mode using the first and second orders of the grating. The velocity resolution of PACS in first order ranges from ≈320 to 180 km s^{-1} over the wavelength range from 105 to 190 μm, and in second order from ≈210 to 110 km s^{-1} from 52 to 98 μm. The data reduction was performed using the PACS reduction and calibration pipeline (ipipe) included in HIPE 14.0.1, with calibration tree version 72, using an oversampling of four fully independent channels (an upsample parameter of 1). The molecular absorption lines are effectively point-like in ESO 320-G030, and we have thus used the point source calibrated spectra "c129" produced by scaling the emission from the central ≈9″ × 9″ spatial pixel to the total emission from the central 3 × 3 spaxels ("c9"), which is itself scaled according to the point-source correction (see also González-Alfonso et al. 2017). The absolute flux scale is robust to potential pointing jitter, with continuum flux reproducibility of ±15%. The H_2O spectra observed with *Herschel*/PACS toward ESO 320-G030 are shown in Fig. 2, together with the adopted baselines and Gaussian fits to the profiles. The resulting line fluxes along with transition parameters are listed in Table 1. The individual H_2O lines are denoted according to their round-off wavelengths as indicated in the second column of Table 1, except the line observed with ALMA that is denoted according to its frequency in GHz (i.e., H_2O448).

All observed H_2O lines in the PACS wavelength range (57−145 μm) are detected in absorption, as also seen in several other buried galactic nuclei (e.g., González-Alfonso et al. 2004, 2008, 2012; Fischer et al. 2014). Lower level energies cover a full range of 61 to 644 K, and are thus expected to probe regions with significantly different dust temperatures ($T_{\rm dust}$). Specifically, the highest-lying line H_2O72 is clearly detected, indicating the presence of a very warm, optically thick component in the nucleus of ESO 320-G030 (Pereira-Santaella et al. 2017).

2.2. Herschel/SPIRE data

The *Herschel*/SPIRE (Griffin et al. 2010) spectrum of ESO 320-G030 was obtained as part of the *Herschel* Open Time Key Project *Hercules* (PI: P. van der Werf). The SPIRE spectrometer observations cover the wavelength range 191−671 μm with two spatial arrays covering two bands: SSW (191−318 μm) and SLW (294−671 μm). The HIPE 15.0.1 unapodized spectra were downloaded from the archive, with a spectral resolution of full-width half-maximum $FWHM$ (km s^{-1}) = 1.4472 $\lambda(\mu$m). The observed lines are indicated with green arrows in Fig. 1, and the spectra are shown in Fig. 3. Sinc functions on top of baselines of order 1 were fitted around the spectra, and the resulting line fluxes are also listed in Table 1.

As observed in all other (U)LIRGs at low and high redshifts (e.g., González-Alfonso et al. 2010; Yang et al. 2013, 2016; Liu et al. 2017; Lis et al. 2011; Pereira-Santaella et al. 2013; Omont et al. 2013), the excited submillimeter lines of H_2O (i.e., with the lower level of the transition above ground-state) are observed in emission. Only the ground-state H_2O $1_{11} - 0_{00}$ (H_2O269) line is observed either in emission and/or absorption, depending on the source (González-Alfonso et al. 2010; Spinoglio et al. 2012; Weiß et al. 2010; Rangwala et al. 2011), with complex intrinsic profiles in some galaxies as observed with the high-resolution *Herschel*/HIFI spectrometer (Liu et al. 2017). In ESO 320-G030, the H_2O269 line is seen in absorption but significantly redshifted relative to the other lines. This redshifted absorption is also seen in other ground-state transitions, as the OH doublets at 119 and 79 μm, tracing an apparent extended inflow (González-Alfonso et al. 2017). Cancellation of emission and absorption features in the H_2O269 line within the SPIRE spectral resolution cannot be ruled out. The ground-state H_2O^+ $1_{11} - 0_{00}$ 3/2 − 1/2 line at 268.85 μm, detected in strong absorption in M82 (Weiß et al. 2010), is not detected in ESO 320-G030.

The H_2O lines displayed in Fig. 3 are the same as those detected with *Herschel*/SPIRE toward Mrk 231 (González-Alfonso et al. 2010). The lines in this wavelength range that trace the warmest dust are the high-lying H_2O248 and H_2O212 transitions. In Mrk 231, the flux ratio of these lines is $H_2O212/H_2O248 \approx 0.8$, while this ratio in ESO 320-G030 is significantly lower, ≈0.4. Since the H_2O212 line requires warmer dust than the H_2O248 to be efficiently excited, the lower ratio in ESO 320-G030 indicates lower $T_{\rm dust}$ than in Mrk 231 in the region sampled by these lines (Sect. 3.2.2).

2.3. ALMA data

In the present study we use a new reduction of the band 8 ALMA data of ESO 320-G030 based on the combination of extended and compact array configurations. The observations

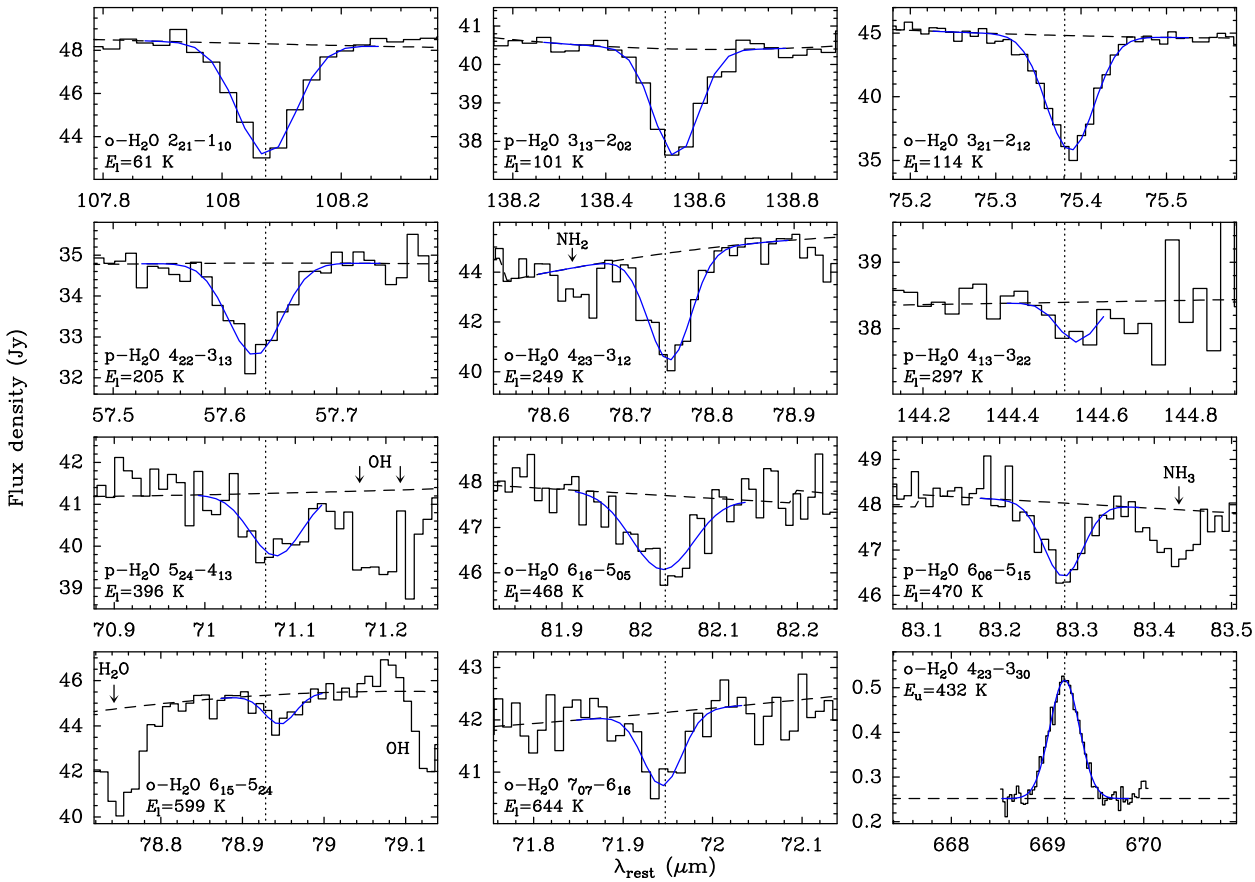

Fig. 2. Spectra around the H_2O lines in ESO 320-G030 observed with *Herschel*/PACS and ALMA (*lower-right panel*), along with Gaussian fits to the lines (blue curves). In all panels, the plotted wavelength range corresponds to a velocity range of ±800 km s^{-1}. The adopted baselines are shown with dashed lines. The vertical dotted lines indicate the expected central position of the lines by using z = 0.010266, which is derived from the Gaussian fit to the H_2O448 line observed with ALMA. The *Herschel* lines are sorted by the lower-level energy (E_l) of the transition, which is also indicated in each panel. The species responsible for other lines in the spectra are also indicated (see also Appendix A).

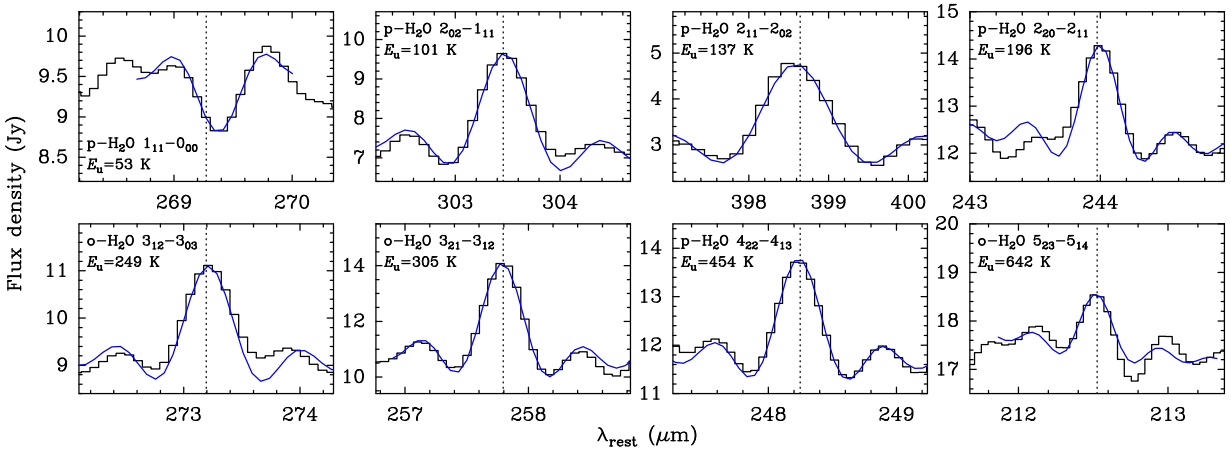

Fig. 3. Spectra around the H_2O lines in ESO 320-G030 observed with *Herschel*/SPIRE, along with sinc fits to the lines (blue curves). In all panels, the plotted wavelength range corresponds to a velocity range of ±1200 km s^{-1}. The vertical dotted lines indicate the expected central position of the lines by using z = 0.01026, as in Fig. 2. The lines are sorted by the upper-level energy (E_u) of the transition, which is indicated in each panel.

with the extended configuration (project #2016.1.00263.S), with baselines ranging from 15 to 920 m, 42 antennas and a maximum recoverable scale of ∼2″, were described in Pereira-Santaella et al. (2017). The compact configuration has baselines from 15 to 160 m, providing a maximum recoverable scale of ∼6″. The two data sets were calibrated using the standard ALMA reduction software CASA (version 5.4; McMullin et al. 2007), and combined in the uv plane within the LRSK frequency reference frame. For spectroscopic observations of the H_2O448 line, a velocity resolution of ≈10 km s^{-1} (≈16 MHz) was selected in the final data cubes, as well as pixels with a size of 0.06″. We used for the cleaning the Briggs weighting with a robustness parameter of 0.5 (Briggs 1995), which provided a beam with a full width at half maximum (FWHM) of

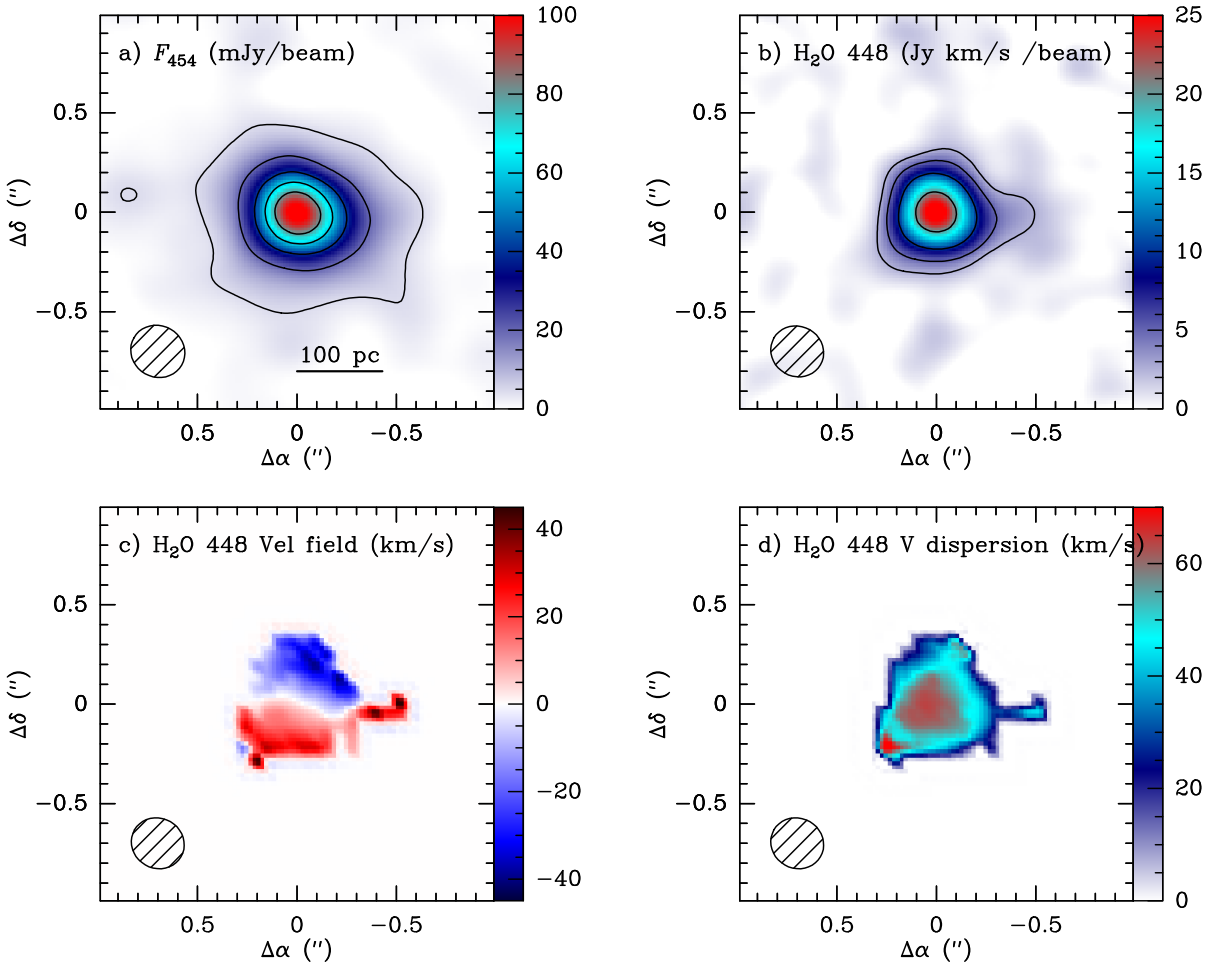

Fig. 4. ALMA maps of the continuum at 454 GHz (660 μm, *panel a*), and of the integrated intensity (moment 0, *panel b*), velocity field (moment 1, *panel c*), and velocity dispersion (moment 2, *panel d*) of the H_2O448 line. North is up and east is left. The rms noise is 1.4 mJy beam^{-1} in *panel a* and 0.8 Jy km s^{-1} beam^{-1} in *panel b*. Contours are 4.5 (≈3σ), 20, 40, 60, and 80 mJy beam^{-1} in *panel a*, and 2.5 (≈3σ), 5, 10, and 20 Jy km s^{-1} beam^{-1} in *panel b*. The hatched ellipses indicate the synthesized beam.

0.27 × 0.25 arcsec^2 (63 × 58 pc^2) and a position angle (PA) of ≈ 60 deg. The resulting 1σ sensitivity was of ≈6 mJy beam^{-1} for the 16 MHz channels. The continuum was extracted from line-free channels in the upper sideband at 454 GHz. With a similar beam size and PA as for the line observations, the achieved 1σ sensitivity was of ≈1.4 mJy beam^{-1}.

The spectrum of the H_2O448 line extracted from a circular aperture of radius 0.48″ is shown in the lower-right panel of Fig. 2, yielding a flux of 44.5 ± 1.2 Jy km s^{-1}. The maps of the 454 GHz (660 μm) continuum, which is dominated by thermal dust emission (Pereira-Santaella et al. 2016, 2017), and of the velocity-integrated intensity (moment 0), velocity field (moment 1), and velocity dispersion (moment 2) of the H_2O448 line are shown in Fig. 4. The 454 GHz continuum flux extracted from an aperture of radius 0.9″ is 260.1 ± 1.7 mJy. The fluxes measured in the H_2O448 line and continuum are slightly higher than previously reported (Pereira-Santaella et al. 2017) because of the inclusion of the compact array configuration.

As noted in Pereira-Santaella et al. (2017), the 454 GHz continuum, with a low-brightness surface above 3σ level of 0.83 arcsec^2 (effective radius of 120 pc), is significantly more spatially extended than the H_2O448 line, which probes a nuclear disk (Fig. 4c). The maps of both the continuum and H_2O448 line are elongated in approximately the east-west direction, in contrast with the CO (2−1) emission that traces much larger scales and probes a disk inclined i = 43° and with PA = 133° (Pereira-Santaella et al. 2016). The continuum at 454 GHz and the H_2O448 line emission are however aproximately aligned with the nuclear bar (PA = 75°, see Sect. 4.1).

3. Analysis

As shown in Figs. 2 and 3, a total of 20 H_2O lines in absorption or in emission, with wavelengths ranging from 58 to 669 μm, are detected in ESO 320-G030, and an ALMA map of one high-lying line, the H_2O448 transition, is available, as well as the map of the 454 GHz continuum dominated by thermal dust emission. This gives a unique opportunity to combine all these data, and exploit at the maximum level the *Herschel*/ALMA synergy to infer the distribution of luminosity sources, their spatial extent, dust temperatures, and ISM column densities with unprecedented accuracy. To attain this goal, we fit the data, including up to 3 continuum flux densities, to a linear combination of spherically symmetric model components from a library (Sect. 3.1), which yields the solid angles, and hence the spatial scales of the different components. Since H_2O is excited primarily through absorption of dust-emitted photons, our fit also gives specific predictions for the spectral energy distribution (SED) of the fitted components, and the predicted combined SED is compared with the observed SED (Sect. 3.2). In addition, the fit

Table 1. H_2O lines in ESO 320-G030.

Transition	Name	λ_{rest} (μm)	E_{lower} (K)	E_{upper} (K)	Flux (Jy km s^{-1})	Obs ID
p-H_2O $4_{22}-3_{13}$	H_2O58	57.636	204.7	454.3	−700.2 ± 74.5	1342248551
p-H_2O $5_{24}-4_{13}$	H_2O71	71.067	396.4	598.9	−449.7 ± 77.7	1342248549
o-H_2O $7_{07}-6_{16}$	H_2O72	71.947	643.5	843.5	−317.7 ± 55.7	1342248549
o-H_2O $3_{21}-2_{12}$	H_2O75	75.381	114.4	305.3	−2512.2 ± 54.1	1342248549
o-H_2O $4_{23}-3_{12}$	H_2O78	78.742	249.4	432.2	−1076.5 ± 52.5	1342248549
p-H_2O $6_{15}-5_{24}$	H_2O79	78.928	598.9	781.2	−239.0 ± 43.4	1342248549
o-H_2O $6_{16}-5_{05}$	H_2O82	82.031	468.1	643.5	−592.6 ± 64.9	1342248552
p-H_2O $6_{06}-5_{15}$	H_2O83	83.284	470.0	642.7	−370.9 ± 49.5	1342248552
o-H_2O $2_{21}-1_{10}$	H_2O108	108.073	61.0	194.1	−1755.4 ± 75.4	1342248550
p-H_2O $3_{13}-2_{02}$	H_2O138	138.528	100.8	204.7	−736.7 ± 31.2	1342248550
p-H_2O $4_{13}-3_{22}$	H_2O144	144.518	296.8	396.4	−132.9 ± 37.0	1342248549
o-H_2O $5_{23}-5_{14}$	H_2O212	212.526	574.7	642.4	265.2 ± 18.3	1342210861
p-H_2O $2_{20}-2_{11}$	H_2O244	243.974	136.9	195.9	557.6 ± 25.0	1342210861
p-H_2O $4_{22}-4_{13}$	H_2O248	248.247	396.4	454.3	656.4 ± 26.1	1342210861
o-H_2O $3_{21}-3_{12}$	H_2O258	257.795	249.4	305.3	1013.5 ± 26.9	1342210861
p-H_2O $1_{11}-0_{00}$	H_2O269	269.272	0.0	53.4	−237.4 ± 30.2	1342210861
o-H_2O $3_{12}-3_{03}$	H_2O273	273.193	196.8	249.4	700.1 ± 29.3	1342210861
p-H_2O $2_{02}-1_{11}$	H_2O303	303.456	53.4	100.9	883.0 ± 42.8	1342210861
p-H_2O $2_{11}-2_{02}$	H_2O399	398.643	100.8	136.9	878.4 ± 26.9	1342210861
o-H_2O $4_{23}-3_{30}$	H_2O448	669.178	410.7	432.2	44.5 ± 1.2	ALMA#2016.1.00263.S

enables a Bayesian analysis that yields the probability densities of the inferred physical parameters. To check the reliability of these results, the components inferred from the spherically symmetric models are combined into a physical model in 3D, with predicted maps for the 454 GHz continuum and the H_2O448 line that are compared with the observed maps to further refine our results (Sect. 3.3).

3.1. Fitting procedure

3.1.1. Defining the data set

We attempt to model the nuclear region of ESO 320-G030 from the H_2O absorption and emission lines and the observed continuum flux densities at some specific wavelengths. We include in the fit all detected H_2O lines, which are observed with the *Herschel* beam of ∼9″ (PACS) and ∼20″ (SPIRE). While the high-lying absorption lines are indeed expected to be fully nuclear, this is not necessarily true for the lowest-lying absorption and emission lines. Nevertheless, the low-brightness emission observed in the 454 GHz continuum map (Fig. 4a) indicates the presence of a nuclear but relatively extended (∼150 pc) component where the low-lying absorption and emission can be formed. We will thus implicitly assume that all H_2O lines with a non-ground-state lower level ($E_{lower} > 0$) are basically nuclear and associated with the spatial scale of the 454 GHz map, and results below will show the plausibility of this assumption.

Nevertheless, we note that the ground-state H_2O269 line, the only SPIRE line that is seen in absorption, is significantly redshifted relative to the systemic velocity (Fig. 3), similar to the OH ground-state lines at 119 and 79 μm (González-Alfonso et al. 2017). On the one hand, such absorption is expected to be produced by foreground gas not necessarily forming part of the modeled nuclear gas. On the other hand, an inner strong emission line is disfavored because there is no hint of an emission feature in the blueshifted part of the line. We therefore include the line in the fit with a high 1σ uncertainty of 200 Jy km s^{-1}, nearly the value of the measured flux (Table 1). In addition, the very high-lying H_2O $8_{18}-7_{07}$ line at 63.32 μm, lying close to the [O I] 63 μm line, is detected in NGC 4418 (González-Alfonso et al. 2012), but is not detected in ESO 320-G030, with <70 Jy km s^{-1} (2σ). We also use below this non-detection to further constrain the inferred physical parameters of the core of the nucleus (Sect. 3.1.5).

We consider in the fit 3 continuum flux densities, at 30, 428, and 660 μm, as constraints for fitting the SED. The measured flux densities at 428 μm (700 GHz, 1.00 ± 0.05 Jy, Pereira-Santaella et al. in prep.) and 660 μm (454 GHz, Fig. 4) are evidently nuclear as they have been measured with ALMA. We also expect the 30 μm continuum as measured by *Spitzer* to be nuclear as well and intrinsically related to H_2O because H_2O probes the SED transition from mid- to far-IR wavelengths (González-Alfonso et al. 2012; Falstad et al. 2015, 2017; Aladro et al. 2018). No more continuum flux densities (e.g., in the far-IR) are included in the fit because they may be contaminated by extended emission unrelated to H_2O.

3.1.2. A library of model components

A library of model components has been developed following the method described in González-Alfonso et al. (2014a). In short, the model components consist of spherically symmetric distributions of gas and dust, for which the statistical equilibrium populations of the H_2O rotational levels are calculated through nonlocal, non-LTE radiative transfer calculations. The fluxes and profiles of all involved lines and the SED of the dust continuum from the mid-IR to the mm are subsequently computed. We assume for each component uniform physical properties: T_{dust}, the continuum optical depth at 100 μm along a radial path τ_{100}, the column density of H_2O along a radial path N_{H2O}, the H_2 density n_{H2}, the velocity dispersion ΔV, and the gas temperature

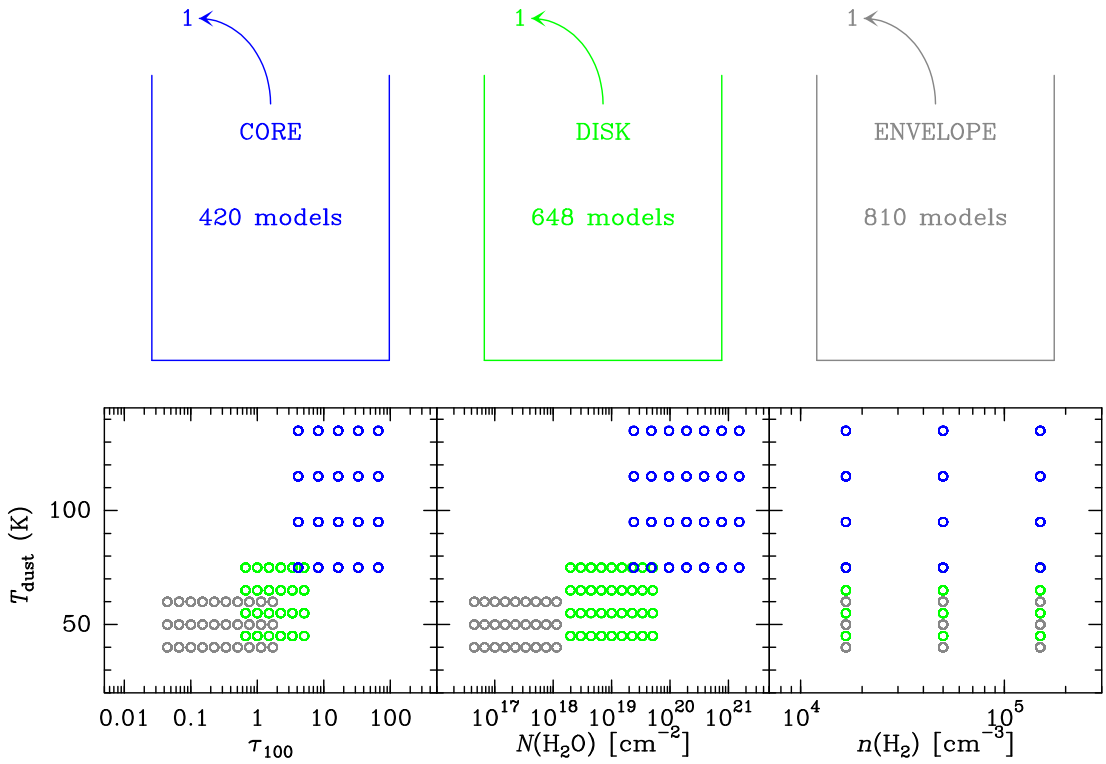

Fig. 5. Spherically symmetric model components are clasified into three groups, the "core" (in blue), the "disk" (in green), and the "envelope" components (in gray), according to their physical parameters. The *lower panels* show the physical parameters, namely, $T_{\rm dust}$, τ_{100}, $N_{\rm H2O}$, and $n_{\rm H2}$, covered by each group of components. Our models for ESO 320-G030 use one component from each group, yielding $\approx 2.2 \times 10^8$ combinations. For each combination, χ^2 is minimized to give the solid angle subtended by each component.

$T_{\rm gas}$. The gas and dust are assumed to be mixed. The physical parameters that are modified from model to model are $T_{\rm dust}$, τ_{100}, $N_{\rm H2O}$, and $n_{\rm H2}$, and we keep fixed $\Delta V = 100\,{\rm km\,s^{-1}}$ and $T_{\rm gas} = 150\,{\rm K}$. As shown in González-Alfonso et al. (2014a), the excitation depends on $N_{\rm H2O}/\Delta V$ and line fluxes are then proportional to ΔV, so that results can be easily scaled to any other value of ΔV.

While the excitation of H_2O is dominated by radiative pumping, and thus our data are much more sensitive to the parameters defining the radiation field ($T_{\rm dust}$ and τ_{100}) than to the collisional parameters ($T_{\rm gas}$ and $n_{\rm H2}$), collisional excitation can still have an impact in populating the low-lying (excited) levels from which the pumping cycle operates (González-Alfonso et al. 2014a). A significant role of H_2O excitation through collisions is not a priori expected in ESO 320-G030 given the lack of emission in the H_2O269 ground-state line (contrary to the case of NGC 1068), but we aim to further check this point by looking for any trend in the line ratios that would favor some role of collisions. To do this, we vary $n_{\rm H2}$ keeping $T_{\rm gas} = 150\,{\rm K}$ as a constant fiducial value characterizing warm (shocked) molecular gas, so that any significant impact of collisions would be reflected in a trend favoring high values of $n_{\rm H2}$. That we do not find such a trend below (Sect. 3.2.2) indicates that our results are insensitive to our choice of $T_{\rm gas}$.

3.1.3. Groups of model components

The model components are classified into 3 groups according to their physical parameters (Fig. 5). The "core" models are all optically thick in the far-IR ($\tau_{100} \geq 4$) and very warm ($T_{\rm dust} \geq 75\,{\rm K}$). The "disk" models have lower τ_{100} but are still (nearly) optically thick ($\tau_{100} \geq 0.7$) with $T_{\rm dust} = 45 - 75\,{\rm K}$. The "envelope" models mainly cover optically thin conditions but can reach optically thick values ($\tau_{100} \lesssim 2$), and have moderate $T_{\rm dust} = 40-60\,{\rm K}$. Each of these 3 groups covers a regular grid in the free parameters ($T_{\rm dust}$, τ_{100}, $N_{\rm H2O}$, $n_{\rm H2}$). Models were generated and added to each group as needed to obtain reliable likelihood distributions of the above parameters, as shown below. While $N_{\rm H2O}$ is varied by more than 1 dex within each group with multiplicative factors of 1.5−2, the grid for $n_{\rm H2}$ is coarser with only 3 values, representing typical densities of buried galactic nuclei ($(1.7-15)\times 10^4\,{\rm cm^{-3}}$, see Fig. 5).

3.1.4. Minimizing $\chi^2_{\rm red}$

As shown below, a reasonable model fit to the present data set requires the combination of $N_c = 3$ components, one from each group (Fig. 5). We then consider all possible combinations, in a number of 2.2×10^8, that are obtained by taking 1 component of each group. For each combination, and since each component j yields line fluxes and continuum flux densities that are proportional to the solid angle $\Delta\Omega_j = \pi R_j^2/D^2$, where R_j is the effective radius, the reduced χ^2 ($\chi^2_{\rm red}$) is minimized to give $\Delta\Omega_j$:

$$\chi^2_{\rm red} = \frac{1}{N_L - N_c} \sum_{i=1}^{N_L} \frac{1}{\sigma_i^2} \left[\left(\sum_{j=1}^{N_c} s_{ji}^{\rm comp} \Delta\Omega_j \right) - S_i^{\rm obs} \right]^2 , \quad (1)$$

where $N_L = 24$ is the number of H_2O lines and continuum flux densities that are fitted, $S_i^{\rm obs}$ are the observed fluxes, σ_i are their uncertainties, and $s_{ji}^{\rm comp}$ is the predicted flux per unit solid angle for line i by model component j. To obtain σ_i, we sum in quadrature the errors in Table 1 and the systematic uncertanties of 15% and 10% for the *Herschel* and ALMA measurements,

respectively. The minimization is performed by a standard procedure and yields both R_j for each component of the combination and then the minimum $\chi^2_{\rm red}$.

3.1.5. Likelihood distributions

Our model for ESO 320-G030 has a total of $N_f = 12$ free physical parameters, ($T_{\rm dust}$, τ_{100}, $N_{\rm H2O}$, $n_{\rm H2}$) for each of the 3 model components. In our approach, the sizes R_j for each combination are treated as derived rather than free parameters, as they are uniquely determined from the $\chi^2_{\rm red}$ minimization above. We follow Ward et al. (2003) and Kamenetzky et al. (2011) in calculating the likelihood distributions of the free physical parameters, which are collected into vector $\boldsymbol{a}$. A given set of values $\boldsymbol{a}$ yields modeled line fluxes or continuum flux densities that are inserted into the vector $\boldsymbol{S}(\boldsymbol{a})$ of $N_L = 24$ components. We also denote as vectors $\boldsymbol{S}^{\rm obs}$ and $\boldsymbol{\sigma}$ the values and uncertainties measured for these quantities. For a given set of physical parameters $\boldsymbol{a}$, the probability density for measuring a set of values $\boldsymbol{S}^{\rm obs}$ is

$$P(\boldsymbol{S}^{\rm obs}|\boldsymbol{a},\boldsymbol{\sigma}) = \prod_{i=1}^{N_d} \frac{1}{\sqrt{2\pi}\sigma_i} \exp\left\{-\frac{1}{2}\left[\frac{S_i^{\rm obs} - S_i(\boldsymbol{a})}{\sigma_i}\right]^2\right\} \times \prod_{i=1}^{N_u} \frac{1}{2}\left[1 + {\rm erf}\left(\frac{\sigma_i - |S_i(\boldsymbol{a})|}{\sqrt{2}\sigma_i}\right)\right], \quad (2)$$

where $N_d = 23$ corresponds to the line and continuum detections and $N_u = 1$ to the undetected H_2O $8_{18} - 7_{07}$ line at 63.32 μm, which is treated according to Appendix B by Pereira-Santaella et al. (2015).

The likelihood of a particular set of parameters $\boldsymbol{a}$, for a set of measurements $\boldsymbol{S}^{\rm obs}$, is given by the Bayes's theorem:

$$P(\boldsymbol{a}|\boldsymbol{S}^{\rm obs},\boldsymbol{\sigma}) = \frac{P(\boldsymbol{a})\,P(\boldsymbol{S}^{\rm obs}|\boldsymbol{a},\boldsymbol{\sigma})}{\int {\rm d}\boldsymbol{a}\,P(\boldsymbol{a})\,P(\boldsymbol{S}^{\rm obs}|\boldsymbol{a},\boldsymbol{\sigma})}, \quad (3)$$

where $P(\boldsymbol{a})$ is the prior probability density function. The posterior distribution of Eq. (3) is marginalized over to obtain the likelihood distribution of a specific parameter a_i, and of any function of parameters $f(\boldsymbol{a})$ (Eqs. (5) and (6) in Ward et al. 2003).

Besides calculating the probability densities of the $N_f = 12$ free parameters, we also determine for each component the likelihood distributions for the sizes R_j, the H_2O abundances relative to H nuclei ($X_{\rm H2O} = N_{\rm H2O}/(1.3 \times 10^{24}\tau_{100})$, González-Alfonso et al. 2014a), the infrared luminosities $L_{\rm IR}$, and the fractions of the H_2O448 flux and 454 GHz continuum flux density arising from each component ($f[F(H_2O448\,{\rm GHz})]$ and $f[F(454\,{\rm GHz})]$, respectively).

We started running calculations with the prior probability density function $P(\mathbf{a}) = 1$ for all sets of parameters. We found in this case that some solutions for the disk, characterized by extremely high $N_{\rm H2O}$ and low $T_{\rm dust} < 50$ K, yielded significant likelihood. A similar situation was also found by Ward et al. (2003) in their bayesian analysis of the ^{12}CO emission in M82, where solutions with unphysically large CO column densities and low volume densities were rejected. We have then put a single constraint on the H_2O abundance as derived above from $N_{\rm H2O}$ and τ_{100}, which implicitly assumes a gas-to-dust ratio of 100 by mass. Models that have accounted for the H_2O absorption and emission in buried galactic nuclei have shown that high H_2O abundances are inferred in the very warm nuclear cores with $T_{\rm dust} \gtrsim 90$ K (González-Alfonso et al. 2012; Falstad et al. 2015, 2017; Aladro et al. 2018). However, in the more extended regions surrounding these cores where $T_{\rm dust}$ is moderate, $X_{\rm H2O}$ decreases to values $<10^{-5}$. To avoid unphysical solutions of extremely high $X_{\rm H2O}$ in moderately warm environments, we use the prior $P(\boldsymbol{a}) = 0$ whenever a model component with $T_{\rm dust} < 60$ K and $X_{\rm H2O} > 3 \times 10^{-5}$ is found, and $P(\boldsymbol{a}) = 1$ otherwise.

3.2. Results

The values of $\chi^2_{\rm red}$ for the best-fit 10^3 combinations are in the range 1.0–1.4, indicating that three components provide a good fit and more are not needed. On the other hand, the minimum value of $\chi^2_{\rm red}$ significantly increases to 2.3 when only 2 components are used. Based on the superior comparison between the observed and model-predicted maps of the H_2O448 and 454 GHz continuum emission (see Sect. 3.3), we have selected a specific model combination, with $\chi^2_{\rm red} = 1.098$, as the fiducial model for detailed comparison with the data. Results for the fiducial model are compared with *Herschel* data and with the observed SED of ESO 320-G030 in Fig. 6, and Fig. 7 displays the probability distributions of the free (upper row) and derived (lower row) parameters. The modeled and observed profiles of the *Herschel*/PACS and ALMA lines, and of the *Herschel*/SPIRE lines are compared in Figs. 8 and 9, respectively. Median likelihood estimators and 90% confidence intervals, together with the values of the parameters of the fiducial model, are listed in Table 2. We also evaluate the degeneracy among the free parameters by showing in Appendix B their marginalized 2D posterior distributions.

3.2.1. The core, disk, and envelope components

As stated in Sect. 3.1.4, we require 3 components to attain a reasonable fit to the whole data set, which can be now justified in the light of Figs. 6a–b and 7. To fit the high-lying absorption lines ($E_{\rm lower} \gtrsim 300$ K) observed with *Herschel*/PACS, a very warm ($T_{\rm dust} \gtrsim 80$ K) and optically thick at 100 μm "core component" is required. Its very small effective size ($R \sim 12$ pc, Fig. 7f) suggests a torus around an AGN, such as that of NGC 1068 (see García-Burillo et al. 2019) but with a much higher column density and mass (Sect. 3.2.5); it could also represent super star clusters in a very early stage of evolution (Rico-Villas et al. 2020) spread over the nuclear region. Because of the compactness of this component, it cannot be solely responsible for the measured fluxes of the rest of H_2O absorption lines. Therefore, the inclusion of a "disk component" is required, with a more moderate $T_{\rm dust} \gtrsim 55$ K but still optically thick in the far-IR ($\tau_{100} \approx 1.5$, Figs. 7a–b). Its size, $R \sim 40$ pc (Fig. 7f), is similar to the size of the disk observed in the H_2O448 ALMA line (Fig. 4c); this line is indeed predicted to be formed in both the core and disk components (Fig. 7h). The disk mainly accounts for most of the observed flux in the absorption lines with $E_{\rm lower} < 300$ K and for the high-lying lines observed with SPIRE in emission (H_2O248 and 212), contributing in addition significantly to many of the remaining lines. However, the disk cannot fully account for the low-lying ($E_{\rm lower} \lesssim 300$ K) emission lines (Fig. 6b), and an extended, optically thin component ($\tau_{100} < 1$) is additionally required. This "envelope component", which is also moderately warm ($T_{\rm dust} \approx 50$ K), is predicted to have a radius of ~130–150 pc (Table 2), similar to the extent of the low-brightness surface seen in the 454 GHz map (Fig. 4a). This consistency in sizes supports our assumption that most of the H_2O low-lying emission observed with *Herschel*/SPIRE is of nuclear origin, although some extra-nuclear contribution to the lowest-lying H_2O lines is not ruled out. The optical depths

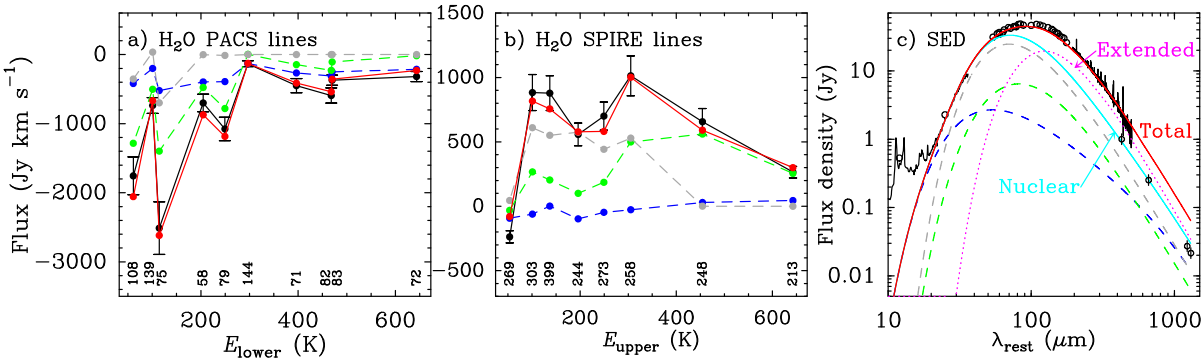

Fig. 6. Our fiducial model fit (with parameters listed in Table 2) to the H_2O PACS lines (*panel a*), H_2O SPIRE lines (*panel b*), and the SED (*panel c*). Dashed blue, green, and gray lines indicate results for the three nuclear components: the core, the disk, and the envelope, respectively. *Panels a–b*: combined (total) absorption or emission of the three components is shown in red, and the small numbers at the bottom indicate the approximate wavelength of the line. *Panel c*: circles at <200 μm show both *IRAS* data and *Herschel*/PACS spectrophotometric data (see Appendix A), with uncertainties better than 15%, and circles with error bars at >400 μm are ALMA data for the nuclear region modeled in this work; we also show the *Spitzer*/IRS and the *Herschel*/SPIRE spectra. The continuum of the combined three nuclear components related to H_2O is shown in light-blue, and a nonnuclear (extended) component (in magenta, with T_{dust} = 28 K) is required to reproduce the full SED at long wavelengths. The red line indicates the total (nuclear+extended) modeled SED.

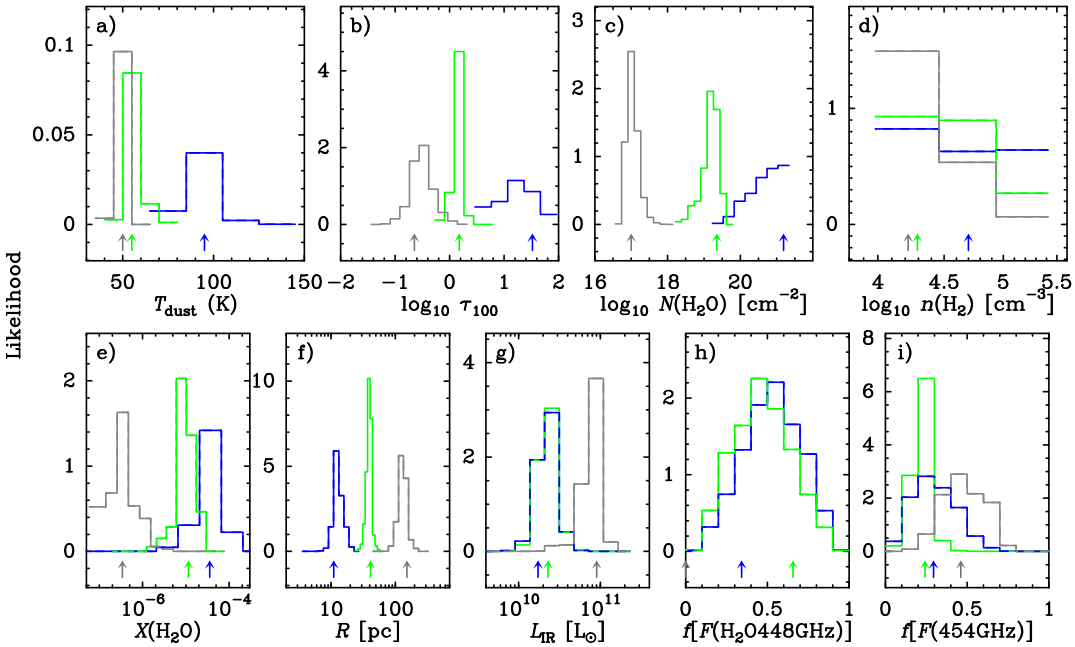

Fig. 7. Bayesian analysis showing the probability densities of the physical parameters associated with the core (blue histograms), disk (green), and envelope (gray). *Panels a–d*: results for the free physical parameters (T_{dust}, τ_{100}, $N(H_2O)$, and $n(H_2)$); *panels e-i*: results for the derived parameters ($X(H_2O)$, R, L_{IR}, and the fractions f of the 448 GHz continuum and of the H_2O448 emission that arise from each component). The small arrows at the bottom of each panel indicate the values of the fiducial model in Fig. 6. In *panel h*, the contribution f to the H_2O448 line from the envelope is not shown because it is negligible in all models. The median and 90% confidence intervals are listed in Table 2.

Table 2. Model results from H_2O multitransition analysis of ESO 320-G030

	Core			Disk			Envelope		
Parameter	Median	Range [a]	Fiducial [b]	Median	Range [a]	Fiducial [b]	Median	Range [a]	Fiducial [b]
T_{dust} (K)	97.3	85.7, 121.0	95.0	54.1	42.9, 59.8	55.0	49.7	45.0, 54.5	50.0
τ_{100}	21.8	4.0, 74.7	32.0	1.5	0.9, 1.8	1.5	0.3	0.1, 0.7	0.22
$\log_{10} N_{H2O}$ (cm^{-2})	20.9	$\gtrsim$20.0	21.2	19.2	18.9, 19.7	19.3	17.0	16.8, 17.5	17.0
$\log_{10} n_{H2}$ (cm^{-3})	4.7	4.1, 5.3	4.7	4.6	4.0, 5.3	4.2	4.4	4.0, 5.1	4.2
R (pc)	11.8	8.9, 15.5 [c]	11.0	41.7	35.0, 54.3	41.4	129.7	91.7, 159.6	130
$\log_{10} L_{IR}$ ($L_\odot$)	10.4	10.1, 10.6	10.2	10.4	10.1, 10.5	10.4	10.9	10.5, 11.0	10.9
$\log_{10} M_{gas}$ ($M_\odot$)	8.1	7.5, 8.7	8.2	8.0	7.7, 8.2	8.1	8.4	8.1, 8.6	8.2
$f[F(H_2O448)]$	0.5	0.2, 0.7	0.34	0.5	0.3, 0.8	0.66	0	0.0, 0.1	0
$f[F(454\,GHz)]$	0.3	0.1, 0.5	0.29	0.2	0.1, 0.4	0.24	0.5	0.2, 0.7	0.47
$\log_{10} X_{H2O}$	−4.5	−5.1, −3.9	−4.36	−5.0	−5.3, −4.4	−4.85	−6.5	−7.0, −5.8	−6.38

Notes. [a]90% confidence intervals. [b]Values for the fiducial model, selected for detailed comparison with data (see Sect. 3.2). [c]Assuming ΔV = 100 km s^{-1} for the core component.

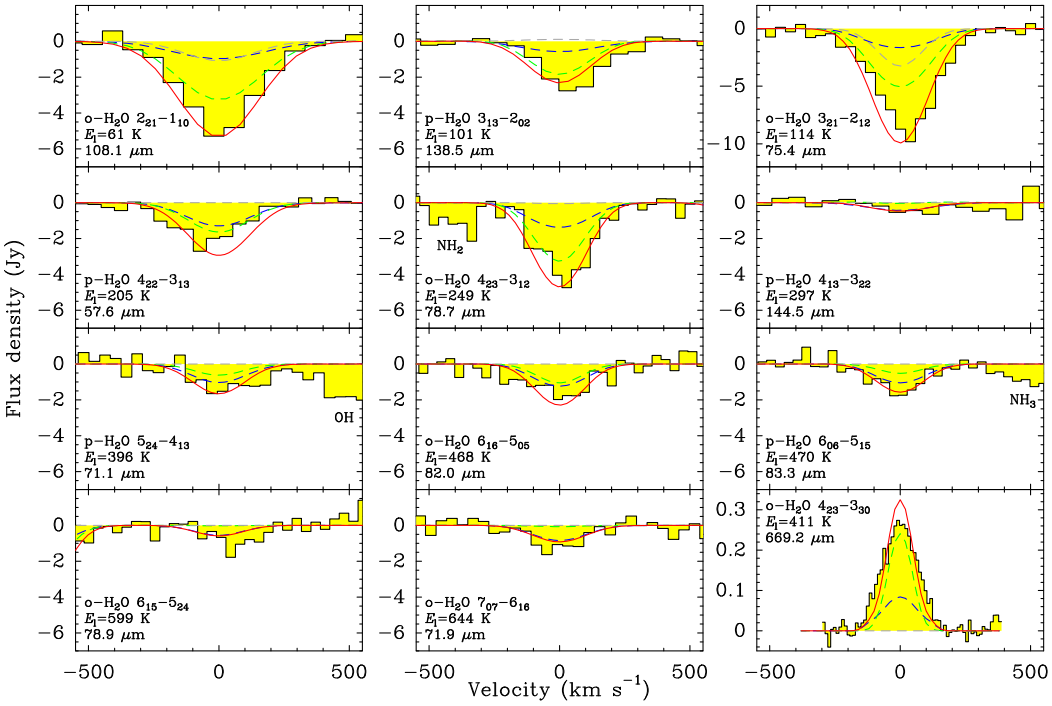

Fig. 8. Fiducial model fit to the H_2O PACS, and ALMA lines. Black histograms show the observed continuum-subtracted spectra, and dashed curves show the contribution by the core component (blue), the inner disk (green), and the outer component (gray). The total predicted absorption or emission is shown in red. Spectral features due to NH_2, OH, and NH_3 lying in the plotted wavelength ranges are also indicated (see Appendix A).

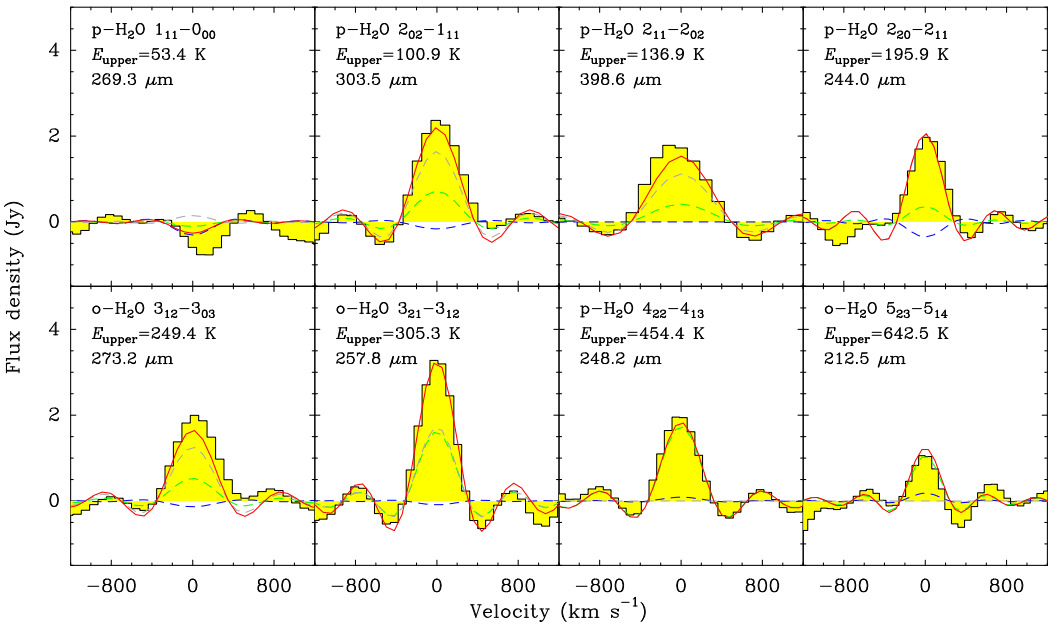

Fig. 9. Fiducial model fit to the H_2O SPIRE lines. Black histograms show the observed continuum-subtracted spectra, and dashed curves show the contribution by the core component (blue), the inner disk (green), and the outer component (gray). The total predicted absorption or emission is shown in red.

at 100 μm, sizes, and H_2O column densities of the three components have distributions with little overlap (Figs. 7b-c-f), which supports the reliability of our three model components approach.

3.2.2. H_2O excitation, column densities, and abundances

While our model grid only explores results for a fixed T_{gas} = 150 K and 3 (expectedly representative) values of n_{H2}, Fig. 7d indicates that the excitation of H_2O is dominated by radiative pumping: The flat distribution in densities for the core indicates that results for this component are insensitive to n_{H2}; for the envelope, results strongly favor low n_{H2}, and low or moderate densities of several $\times 10^4$ cm^{-3} are favored for the disk. We expect that T_{gas} varies across the different components, and that the derived densities would be higher than suggested by Fig. 7d if T_{gas} were lower than assumed. Our models, however, do not

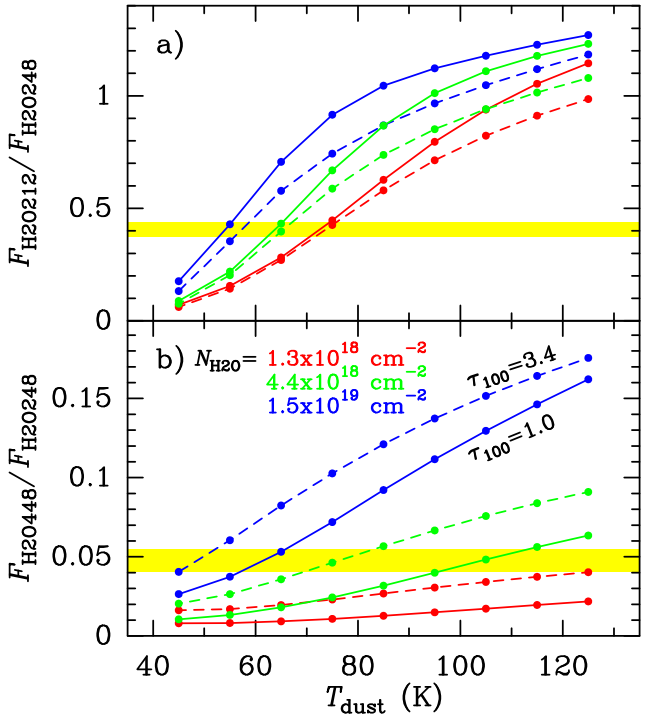

Fig. 10. Modeled H_2O line ratios as a function of T_{dust} (colored lines), compared with the measured ratios (appropriate for the disk, in yellow). The colors indicate the H_2O column densities as indicated in *panel b*, and solid and dashed lines correspond to τ_{100} = 1.0 and 3.4, respectively. *Panel b*: the measured F_{H2O448}/F_{H2O248} has been corrected by assuming that 70% of F_{H2O448} arises from the disk. While the observed $F_{H2O212}/F_{H2O248} \approx 0.4$ ratio in panel a can be explained with a range of T_{dust} and N_{H2O} (increasing T_{dust} with decreasing N_{H2O}), the measured F_{H2O448}/F_{H2O248} breaks the degeneracy favoring the highest N_{H2O} and moderate $T_{dust} \lesssim 65$ K.

require the use of a varying T_{gas} because collisional excitation does not appear to play a key role in the excitation of H_2O.

The column densities N_{H2O} of the envelope and disk components are well defined and very different, $\sim 10^{17}$ and $\sim 10^{19}$ cm^{-2} respectively (Fig. 7c). Estimating the H column densities from the continuum optical depth at 100 μm, the resulting abundances X_{H2O} are $\sim 3 \times 10^{-7}$ and $\sim 10^{-5}$ for the envelope and the disk, respectively.

The disk component, which has high N_{H2O} and is optically thick in the far-IR, nevertheless has a moderate $T_{dust} \approx 55$ K. Since the H_2O248 and H_2O212 emission lines are expected to arise predominantly from the nuclear disk (Figs. 6b and 9), we use their ratio in Fig. 10a to better demonstrate the origin of the physical conditions inferred for this component. The measured H_2O212-to-H_2O248 flux ratio of $\approx$0.4 is by itself consistent with a range of $T_{dust} \approx 55-75$ K depending on N_{H2O}, with T_{dust} decreasing with increasing N_{H2O}. This degeneracy is broken when considering the H_2O448 line observed with ALMA. The measured H_2O448-to-H_2O248 flux ratio in Fig. 10b has been corrected to account for only the fraction of the H_2O448 flux, $\approx$70%, arising from the disk (see Sect. 3.3.3). Even with this correction, the resulting ratio of $\approx$0.048 is so high that it cannot be explained with the lowest $N_{H2O} = 1.3 \times 10^{18}$ cm^{-2} considered in Fig. 10b, but requires higher columns. The highest $N_{H2O} = 1.5 \times 10^{19}$ cm^{-2} and $T_{dust} \approx 55$ K are mostly consistent with both ratios displayed in Fig. 10, although the increase in τ_{100}, as favored in Appendix A, would also enable warmer $T_{dust} \sim 65$ K and lower $N_{H2O} \sim 5 \times 10^{18}$ cm^{-2}. The inferred extremely high N_{H2O} in the disk is consistent with the strong absorption and emission in the $H_2^{18}O$ and ^{18}OH lines, which still require a low $^{16}O/^{18}O \sim 100$ abundance ratio (Appendix A).

In the core component, only a lower limit for N_{H2O} of $\sim 10^{20}$ cm^{-2} is obtained. Primarily responsible for the very high-lying excitation observed with *Herschel*/PACS H_2O lines in absorption (specifically the H_2O72 line with $E_{lower} = 644$ K), all lines -including the submillimeter H_2O448 transition- are saturated in this component. The values of τ_{100} and X_{H2O} are also rather uncertain for the core given its extremely buried conditions.

3.2.3. The fit to the SED and the nuclear SFR

The SED predicted by our fiducial model, shown in Fig. 6c, is rather representative of all best-fit combinations. In the transition from the mid- to far-IR wavelengths (30–50 μm), the SED is dominated by the optically thin, extended envelope, but the flux densities in the (sub)millimeter from the three components are expected to be comparable. The three nuclear components combined, however, account for a luminosity of $L_{IR} = (1.23 \pm 0.17) \times 10^{11}\ L_\odot$ (light-blue curve in Fig. 6c for the fiducial model), that is, $\sim$70% of the total galaxy luminosity. To fit the whole SED from 20 to 550 μm as observed with *Spitzer* and *Herschel*/PACS and SPIRE, an additional extra-nuclear component has been included in Fig. 6c (magenta curve, labeled extended), with $T_{dust} = 28$ K and $L_{IR} \approx 4 \times 10^{10}\ L_\odot$. ALMA and *Herschel*/SPIRE measure continuum flux densities at 428 μm of $\approx$1 and $\approx$2.5 Jy, respectively, indeed indicating the presence of a continuum component missed by ALMA, also at longer wavelengths (>1 mm, Fig. 6c). This component is expected to be of much larger extent than the nuclear components traced by H_2O, and associated with star formation in the rest of the galaxy. There is indeed prominent Pa-α emission well outside the nuclear region (Alonso-Herrero et al. 2006, see also Sect. 4.1).

Using the Kennicutt & Evans (2012) star formation rate (SFR) calibration of the total IR luminosity, which is based on the works by Murphy et al. (2011) and Hao et al. (2011), the total and nuclear SFR are $\approx$25 and $\approx$18 $M_\odot$ yr^{-1}, respectively. These values also assume that the very optically thick and compact core component is powered by star formation; if we assume that its luminosity is driven by an extremely buried AGN, the nuclear SFR is derived from the IR luminosities of only the disk and envelope to give $\approx$16 $M_\odot$ yr^{-1}. Our inferred nuclear SFR is $\sim$40% higher than the values previously estimated (11–13 $M_\odot$ yr^{-1}; Rodríguez-Zaurín et al. 2011; Pereira-Santaella et al. 2016).

The distribution of infrared luminosities L_{IR} of the three nuclear components, shown in Fig. 7g, indicate rather surprisingly similar values for the compact core and the more extended disk. This could suggest that the disk is to some extent heated by (and reemitting) the radiation coming out from the core. However, the disk cannot surround the core on the front side (as seen from the Earth) because the former is optically thick in the far-IR continuum and hence the core would not be detected in the far-IR H_2O lines. If the disk extends only on the sides of the core, it will only intercept a fraction of the luminosity emitted by the latter, thus limiting the nonlocal heating effect at spatial scales of $\sim$40 pc.

3.2.4. The H_2O448 line and the 454 GHz continuum emission

The relative contributions of the three nuclear components to the 454 GHz total flux density of $\approx$250 mJy ($f[F(454\,\mathrm{GHz})]$) are uncertain. While the contribution by the disk is expected to be

around 25%, the contributions by the core and the envelope show broad distributions (Fig. 7i). This uncertainty is due to the distributions in sizes for the envelope and core, and to the relatively broad distribution found for the optical depth τ_{100} of the core (Fig. 7b). The fiducial model has continuum optical depths at 454 GHz of 1.5, 0.07, and 0.01 for the core, disk, and envelope, respectively.

The relative contributions of the core and disk components to the H_2O448 flux are even more uncertain (Fig. 7h). (The envelope makes a negligible contribution to this line in any case.) Since the H_2O448 line is seen in emission, it is potentially sensitive to the volume of the source (rather than to the surface, as is the case for absorption lines) except when saturated, and its flux also depends on the details of the extinction within the core at 448 GHz. Nevertheless, this ambiguity is solved below (Sect. 3.3) because we have the maps of both the H_2O448 line and 454 GHz continuum emission, which can be compared with predictions from the model combinations.

3.2.5. Gas masses

We calculate the gas mass of each component traced by H_2O as

$$M_{\rm gas} = \pi R^2 \tau_{100} \left(\frac{N_{\rm H}}{\tau_{100}}\right) \mu\, m_{\rm H}, \quad (4)$$

where $N_{\rm H}/\tau_{100} = 1.3 \times 10^{24}\,{\rm cm}^{-2}$ is the gas column per unit optical depth at 100 μm (González-Alfonso et al. 2014a), and $\mu = 1.4$ accounts for He. The computed values are also listed in Table 2. The mass associated with the core component has a large uncertainty because its τ_{100} is not well constrained. Our 3D approach in Sect. 3.3 indicates that its mass likely does not exceed $10^8\,M_\odot$. The combined gas mass of the 3 nuclear components is $4.5^{+1.5}_{-0.6} \times 10^8\,M_\odot$.

The CO 2–1 emission from Pereira-Santaella et al. (2016) has also been used to estimate gas masses. Using the CO emission within the 3σ contour of the 454 GHz emission displayed in Fig. 4a, thus covering accurately the three components traced by H_2O, and assuming the same brightness for the 2–1 and 1 − 0 lines with a ULIRG conversion factor of $\alpha_{\rm CO} = 0.78\,M_\odot/({\rm K\,km\,s^{-1}\,pc^2})$, the gas mass is $3.4 \times 10^8\,M_\odot$. This value is comparable to the mass derived from the H_2O model. The CO 2–1 emission is however much more extended than the 454 GHz contiuum (see Sect. 4.1); the gas masses within radii of 1″, 2″, and 3″ in the plane of the galaxy (233, 466, and 700 pc, respectively) are 4.8×10^8, 6.8×10^8, and $8.3 \times 10^8\,M_\odot$, respectively.

The three components probed by H_2O lie within a radius of $r_{\rm H_2O} = 0.9''$ (≈200 pc) from the galaxy center. The dynamical mass within this radius can be estimated from the rotation curve shown by Pereira-Santaella et al. (2016), which gives $M_{\rm dyn} \sim 2.1 \times 10^9\,M_\odot$ (Pereira-Santaella et al., in prep). Using the combined gas mass as derived above from the H_2O model, the gas fraction is $f_{\rm g} = M_{\rm gas}/M_{\rm dyn} \sim 20\%$. At the current rate of nuclear star formation (Sect. 3.2.3), the nuclear starburst has an age of ∼100 Myr. This should be considered an upper limit owing to the plausible presence of a stellar population prior to the current burst.

3.2.6. Summary and limitations of the model

Figure 11 summarizes visually two possible scenarios of the model source based on our three component fitting of the nuclear region of ESO 320-G030. The most extended component, the envelope, has a luminosity of $\sim 8\times10^{10}\,L_\odot$ and an effective radius of ∼130 pc, is optically thin in the far-IR, and only contributes significantly to the absorption or emission of the lowest-lying far-IR and submillimeter lines. Its contribution to the H_2O448 line is negligible, as this line is exclusively formed in environments that are optically thick in the far-IR, the disk and the core. The disk has a luminosity of $\sim 2 \times 10^{10}\,L_\odot$ and an effective radius of ∼40 pc, and contributes significantly to the excited lines of H_2O both in absorption and in emission. Our sketch in Fig. 11 shows the envelope and the disk as ellipses with their major axis coincident with the minor kinematic axis to account for the apparent elongation of the source in that direction, which nearly coincides with the direction of the nuclear bar. The different components can indeed be inclined and shaped arbitrarily provided that the solid angle as derived from our models remains unchanged (ignoring possible significant changes in level populations as a consequence of the different geometry). The disk component is (partially) resolved by the ALMA beam of ≈0.26″. Finally, we identify from the very high-lying absorption lines of H_2O an additional, very compact component with an effective radius of ≈12 pc, very warm ($T_{\rm dust} \sim 100$ K), and with a luminosity similar to that of the disk despite its small size. It is extremely buried with H_2 columns probably above $\sim 10^{25}\,{\rm cm}^{-2}$, resembling the buried galactic nuclei (BGNs) detected in HCN vibrational emission (e.g., Sakamoto et al. 2010; Aalto et al. 2015; Martín et al. 2016). This core is however unresolved by the ALMA beam, and our fit to the H_2O fluxes cannot distinguish between a physically coherent region at the center of the galaxy, as depicted in model A, or a discrete set of star-forming cores spread out over the disk volume (model B) or even beyond. Nevertheless, we can discriminate between both models by comparing the observed spatial distribution of the 454 GHz continuum and H_2O448 emission with the predicted distributions involved by the two scenarios in Fig. 11, as shown below.

3.3. A 3D approach

A 3D model approach is here used with three main purposes: first, to check the reliability of our model fits, and in particular of the calculated sizes of the three components. This is performed by inspecting whether any of our best-fit model combinations, obtained from spherically symmetric models, can predict spatial distributions for the 454 GHz continuum and H_2O448 line emission that are consistent with the ALMA maps. The comparison will provide a way to refine the overall model and discriminate among combinations with low $\chi^2_{\rm red}$, as the contributions by the several model components to the H_2O448 line and to the 454 GHz continuum emission are poorly determined (Figs. 7h–i). Second, we also aim to discriminate between scenarios A and B in Fig. 11. Finally, analysis of the velocity field will establish the dynamical mass as a function of inclination, favoring a given geometric disposition relative to the plane of the galaxy that may shed light on the gas motions responsible for the formation of the nuclear structure.

3.3.1. Description of the 3D model

Our model simulates arbitrarily complex source geometries and velocity fields by means of small cubes defined within a large cube of side 480 pc. The small cubes have sides of 2−3 pc, which determines the resolution of the simulations. While calculations for the equilibrium $T_{\rm dust}$ can be performed with a Monte Carlo approach, we simply use in the present calculations the values of $T_{\rm dust}$ and optical depths (i.e., the brightness), and sizes (i.e., the

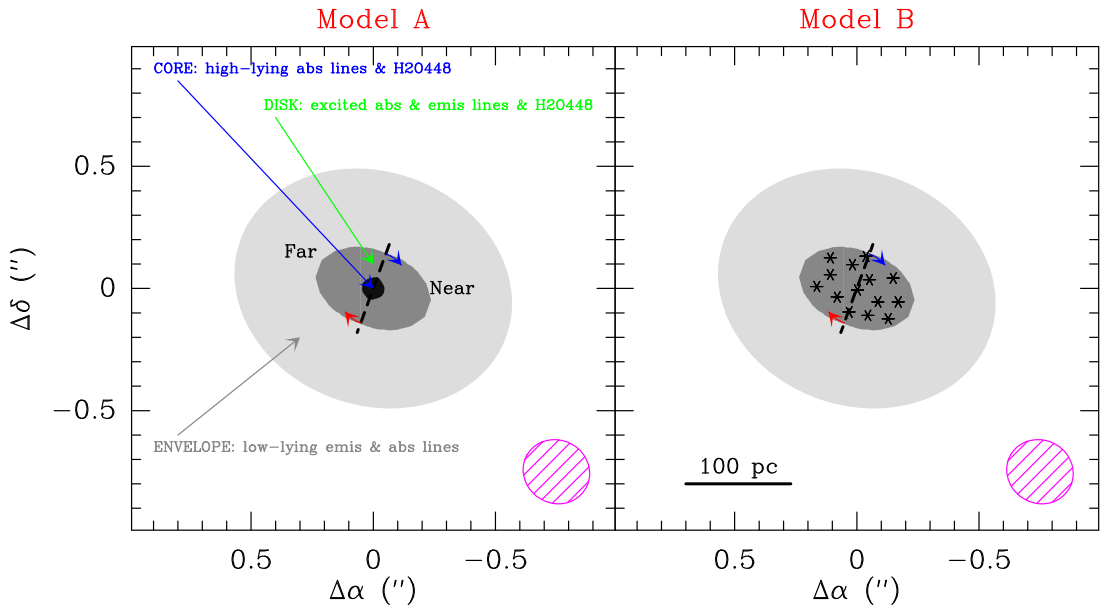

Fig. 11. Two possible sketches of the nuclear region of ESO 320-G030, based on the model fit to the 20 detected and one undetected H_2O lines, and three continuum flux densities. We have in both sketches three components: the compact core, the disk, and the envelope. In *model A*, the core is a physically coherent component located at the center of the galaxy, while in *model B* the core is composed of discrete spots widespread over the disk. The dashed line indicates the major kinematic axis, but the source appears to be elongated along the minor axis that nearly coincidates with the direction of the inner bar. The arrows indicate the clockwise direction of rotation, with far and near sides of the disk also indicated. The envelope is assumed to be fully surrounding the disk.

solid angle) of the three components as inferred from our fiducial model to generate beam-convolved maps at 454 GHz that can be directly compared with the observed maps. Likewise, we use the brightness and solid angle of the H_2O448 line for the core and disk components, as derived from the fiducial model, to generate beam-convolved maps for the H_2O448 line that are compared with the observed spatial distribution.

We use the geometry depicted in Fig. 11. The disk and envelope are assumed to lie in the plane of the galaxy, and are observed with an inclination angle of $i = 43°$ (Pereira-Santaella et al. 2016). The actual sizes for the fiducial model in Table 2 are then increased to match the required solid angles. The kinematic major axis observed in the nuclear region, however, has a PA of 160°, significantly higher than the value of 133° derived from the large-scale CO 2−1 observations (Pereira-Santaella et al. 2016). To approximately account for the elongated shapes along the minor kinematic axis observed in the lowest contours of the 454 GHz continuum and H_2O448 line images (Fig. 4), the disk and envelope are modeled as ellipses with aspect ratio $b/a = 0.6$. The envelope is assumed to cover the disk on the front and back sides, with an effective radius fixed at 130 pc.

The unresolved core component in model A is simulated as a spherical source. In model B, no core is included and the brightness of the disk in both the 454 GHz continuum and the H_2O448 line are increased to match the combined flux of both components.

As pointed out above, there is a wide range in both $f[F(H_2O448)]$ and $f[F(454\,\mathrm{GHz})]$ (i.e., the relative contributions of the different components to the H_2O448 line and 454 GHz continuum emission) among our best-fit solutions (Table 2 and Fig. 7h–i). Our fiducial model was selected because it generates maps for both the 454 GHz continuum and H_2O448 line that compare well with the observed maps, as shown in the next sections.

3.3.2. The 454 GHz continuum

The 3D simulation of the 454 GHz continuum for the fiducial model is compared with the observed map in Fig. 12. Maps of the continuum optical depth at 454 GHz for models A and B are displayed in panels e and f, respectively, and the corresponding intensity maps are shown in panels b and c. The solid angle subtended by each isocontour in panels a–c is shown in panel d.

Our fiducial model reproduces the overall distribution of intensities rather satisfactorily. Specifically, the envelope is required to account for the observed extended emission of the continuum. It is also evident from Fig. 12 that model A more closely resembles the observed map than model B, indicating the presence of an intensity peak of the continuum at the center that we associate with the very high-lying H_2O absorption lines, that is, the core. However, model A slightly overpredicts the intensity continuum from the center. While the model predicts fluxes of 72 and 66 mJy from the core and the disk, a better match to the map would be obtained with ~60 and ~78 mJy, respectively.

3.3.3. The H_2O448 line emission

Only the core and the disk are included in the simulations for the H_2O448 line emission, as the optically thin envelope does not obscure or contribute to this intrinsically weak line. The simulated velocity-integrated intensity maps of the line for models A and B are compared with the observed map in Figs. 13a–c, and the solid angles subtended by the isocontours in these panels are compared in panel d. The emergent line profiles from the whole region are compared with the observed profile in panels e and f, and the observed and modeled intensities along the major and minor axes are compared in the left-hand panel.

From the comparison of the maps, we conclude that an effective disk radius of ≈40 pc matches rather well the observed map.

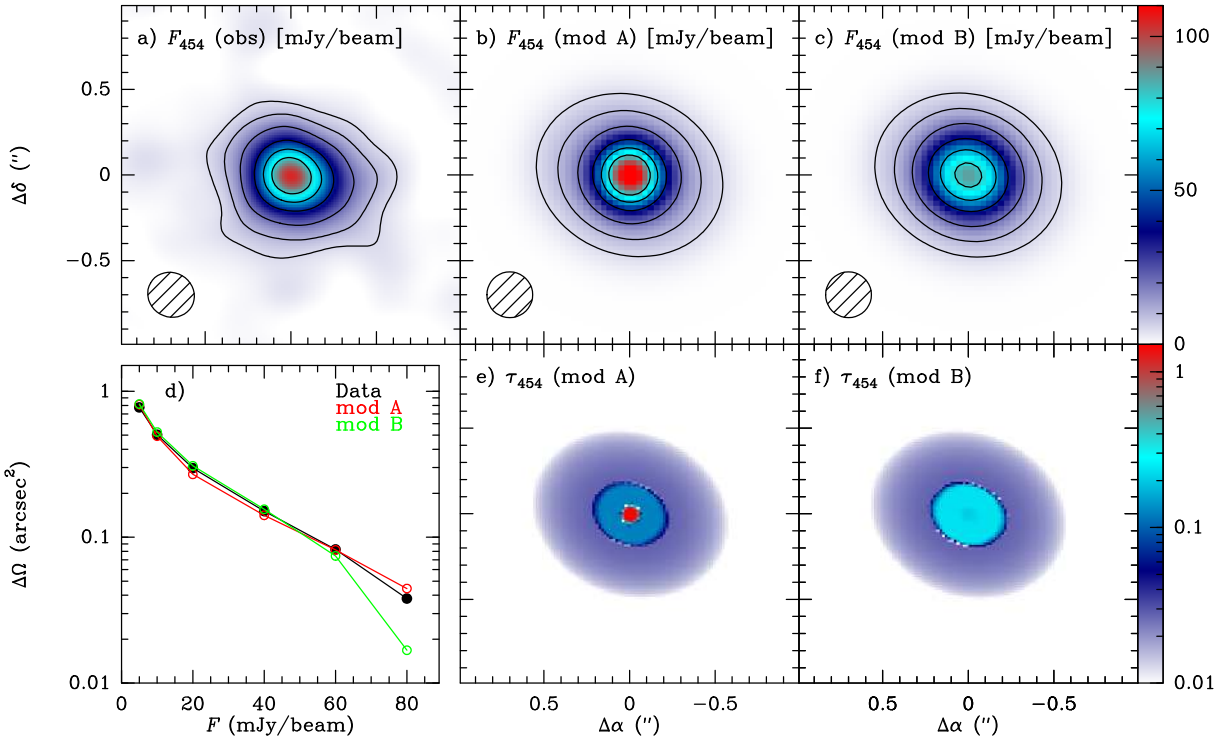

Fig. 12. Comparison between the observed 454 GHz continuum map (*panel a*) and two 3D models (A and B) based on our fiducial model. In model A (*panel b*, with τ_{454} in *panel e*), the core component is assumed to be a real physical component concentrated at the center of the galaxy, and in model B (*panel c*, with τ_{454} in *panel f*), the core component is assumed to be widespread in the inner disk. *Panel d* compares the solid angle subtended by the plotted contours (5, 10, 20, 40, 60, and 80 mJy beam^{-1}) in the observed map (black line and symbols) and in models A and B (red and green, respectively). Model A fits the observed map better than model B.

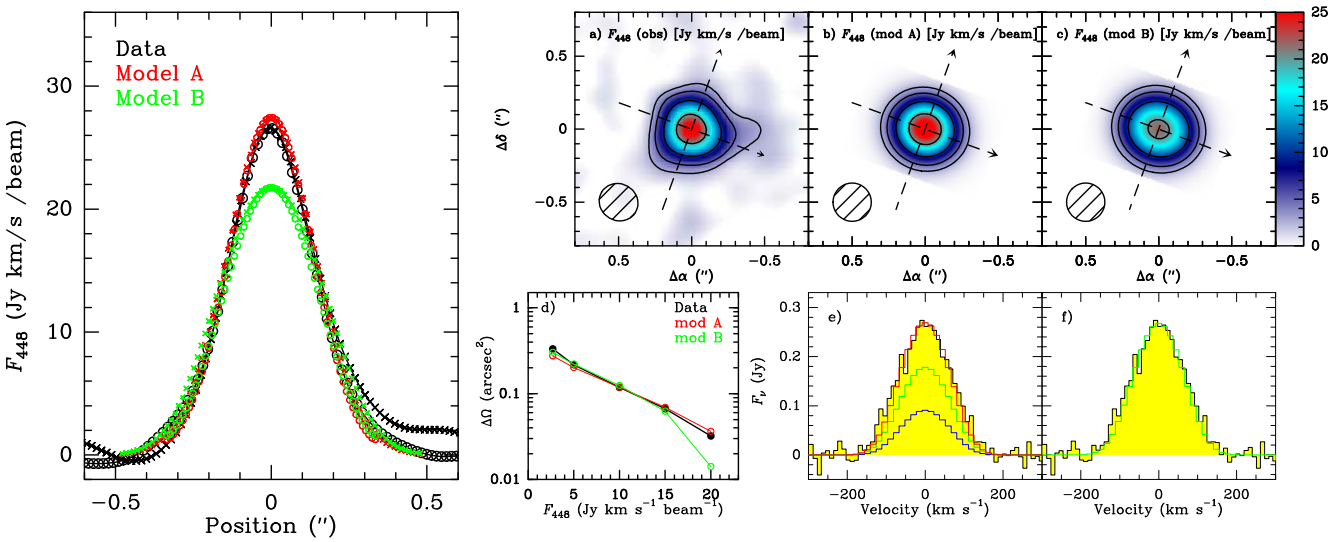

Fig. 13. Comparison between the observed H_2O448 map (*panel a*) and two 3D models (A and B) based on our fiducial model. In model A (*panel b*, with the predicted spectrum in *panel e*), the core component is assumed to be a real physical component concentrated at the center of the galaxy, and in model B (*panel c*, with the predicted spectrum in *panel f*), the core component is assumed to be widespread in the inner disk. *Panel d*: compares the solid angle subtended by the plotted contours (2.7, 5, 10, 15, and 20 Jy km s^{-1} beam^{-1}) in the observed map (black line and symbols) and in models A and B (red and green, respectively). *Left hand panel*: strips in the direction of the two axes indicated in *panels a–c* compare the data to both models. Model A fits the observed map better than model B.

In addition, model A matches the observed intensity distribution slightly better than model B, although higher angular resolution is required to verify this point. In our fiducial model, the core accounts for 13.8 Jy km s^{-1} ($f[F(H_2O448)]$ = 0.31, Fig. 7h) so that the disk dominates the H_2O448 line emission.

3.3.4. The velocity field

The 3D simulations also provide a good match to the observed H_2O448 line shape (Figs. 13e–f). Line broadening is here simulated by both microturbulence, with the same ΔV = 100 km s^{-1} as adopted for the 1D models, and a rotating velocity field that

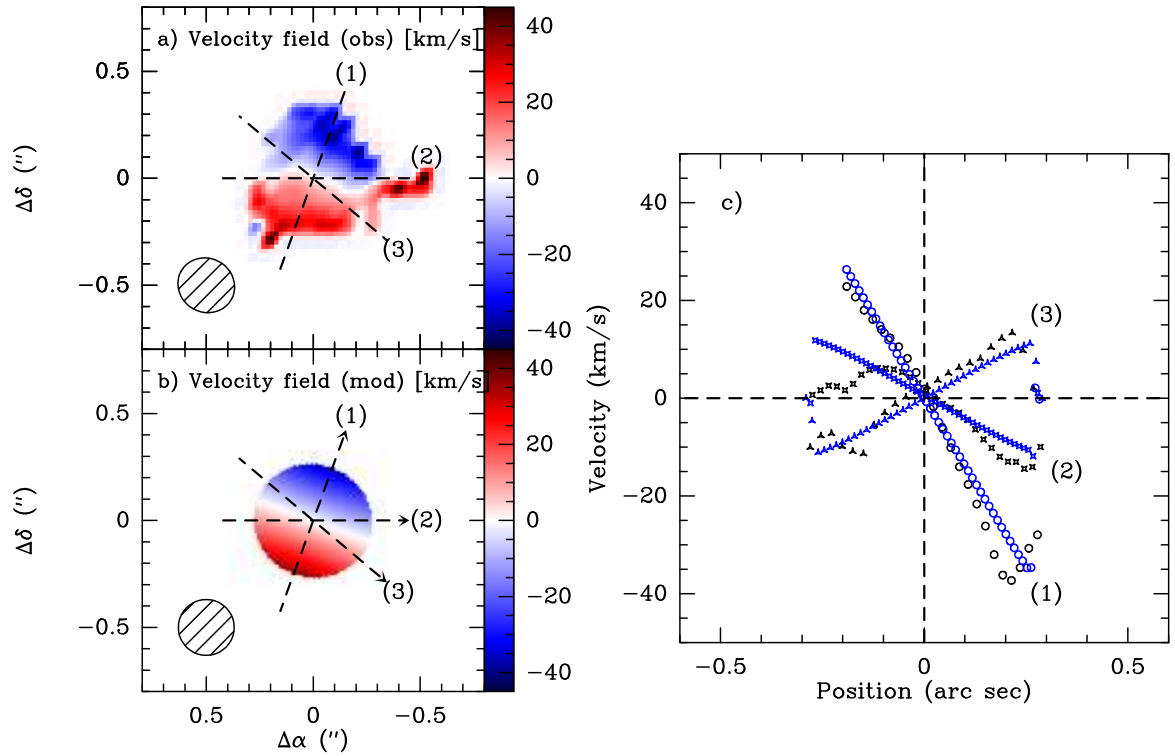

Fig. 14. Velocity field associated with the H_2O448 map (*panel a*) is compared with our 3D model A (*panel b*). The velocity along the three axes indicated in these panels is shown in *panel c*, where black and blue symbols correspond to data and model, respectively.

further broadens the line, of the form:

$$V_{\rm rot}(r < R_{\rm core}) = 100 \times r/R_{\rm core} \quad (5)$$

$$V_{\rm rot}(r > R_{\rm core}) = 100 \ {\rm km\,s^{-1}}, \quad (6)$$

where $R_{\rm core}$ is the radius of the core component. We have not attempted more complex velocity fields given our limited spatial resolution and significant beam smearing. Figure 14 compares the observed and modeled maps of the line-of-sight velocity. Although our adopted velocity field approximately accounts for the observed rotation, the observed field is quite distorted, as is also seen from the strips along the three axes in panel c. The apparent S-shape of the zero velocity contour may indicate an elongated disk (Franx & de Zeeuw 1992) or warping, but also the presence of inflowing gas motions along the minor kinematic axis of the disk. A massive inflow is indeed observed on larger spatial scales, as described below (Sect. 4).

The rotational velocity of $\approx$ 100 km s^{-1} of the disk gives a dynamical mass $M_{\rm dyn}$ that is inconsistent with the high concentration of gas in the nuclear region. Considering both the rotation and dispersion motions as in Bellocchi et al. (2013), $M_{\rm dyn} = 232\, r\, (V_{\rm rot}^2 + 1.35\sigma^2)$ (where the velocities are in km s^{-1} and r in pc) gives $1.4 \times 10^8\ M_\odot$ at $r = 40$ pc, while the combined gas mass (i.e., not including the stellar mass) of the core and disk components is $\sim 2 \times 10^8\ M_\odot$ (Sect. 3.2.5). This discrepancy can be attributed to a lower inclination of the nuclear disk relative to that of the host galaxy; indeed, the kinematic major axis of the nuclear disk is significantly rotated relative to that of the host, which may suggest some degree of kinematic decoupling. Alternatively, $V_{\rm rot}$ could underestimate $M_{\rm dyn}$ if the nuclear gas is not rotationally supported, but supported by radiation pressure and turbulence.

3.3.5. Additional remarks

While the model with 3 components accounts for the main properties of H_2O448 and continuum emission as observed at 0.25″ (60 pc) resolution, it is obviously very schematic with sharp edges and transitions from one component to the next. In reality, we may expect a smoother transition between the different components, with the envelope representing the optically thin extension of the nuclear disk, and the core a cusp of gas column density and $T_{\rm dust}$ located at the center of the galaxy. On the other hand, the majority of the H_2O absorption lines observed with *Herschel*/PACS have rest wavelengths $\lesssim$110 μm, with only 2 absorption lines observed at longer wavelengths. This means that the continuum optical depth of the disk at 120–200 μm is better probed by species with lines observed in this wavelength range. Our model for the remaining molecular species in Appendix A indeed indicates that τ_{100} (disk) is probably somewhat higher (1.5–3) than in our fiducial model. Finally, we note that the sizes estimated for the different components depend on the assumed velocity dispersion of 100 km s^{-1}. While these sizes and ΔV are well constrained for the disk and envelope given the spatial resolution of our ALMA data and the spectral resolution of the H2O448 line, the size of the compact core is not so well constrained as it would increase with lower ΔV. Higher spatial resolution observations would be required to better constrain the size and kinematics of this component.

4. A massive molecular inflow feeding the nucleus of ESO 320-G030

4.1. The inflow seen in CO 2–1

We have so far analyzed the nuclear (inner ~200 pc) region of ESO 320-G030 by combining the *Herschel* and ALMA H_2O

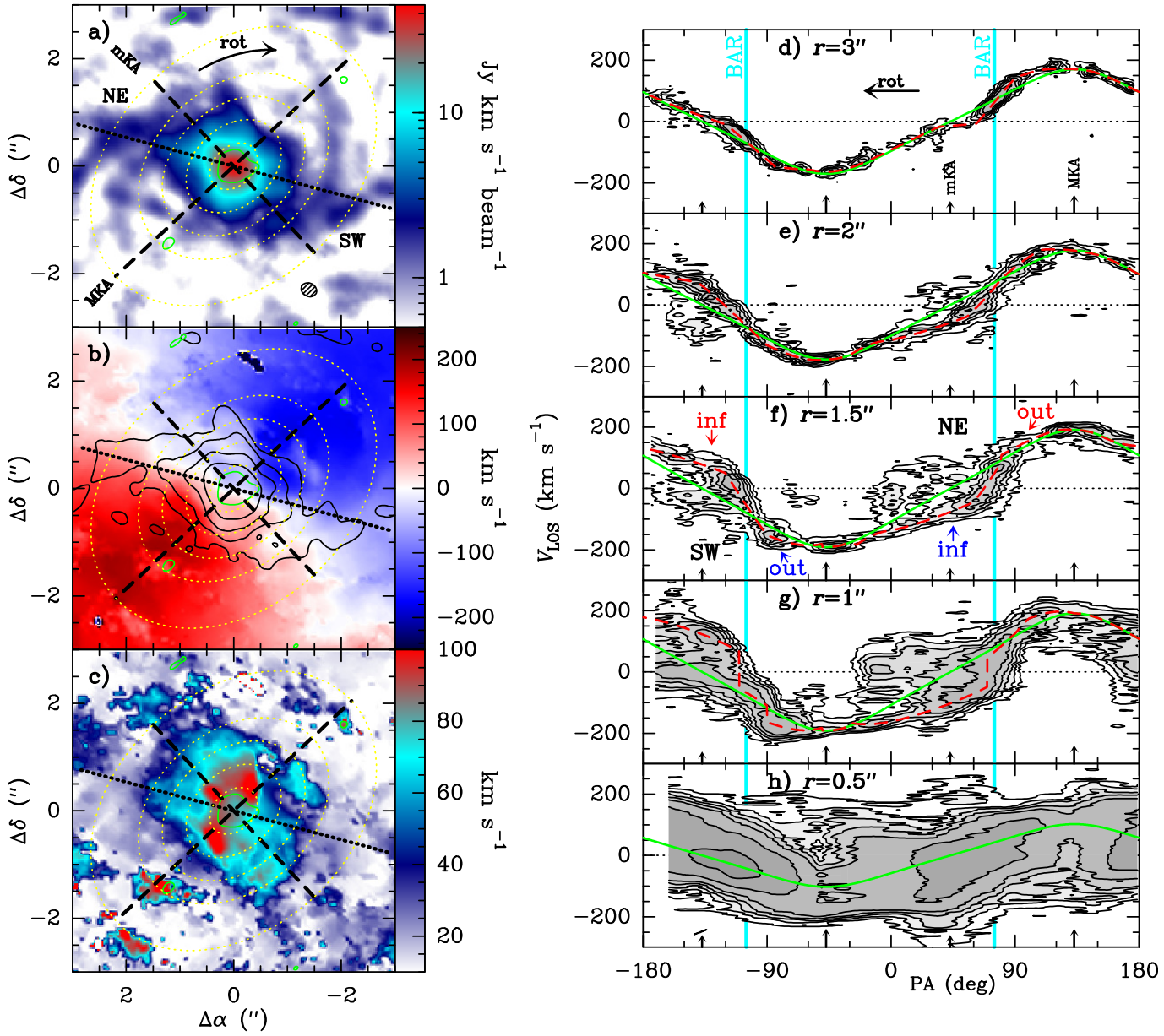

Fig. 15. CO (2–1) emission observed with ALMA in the central region of ESO 320-G030. *Panels a–c* show with colors the integrated intensity (moment 0), velocity field (moment 1), and velocity dispersion (moment 2). The hatched ellipse in *panel a* indicates the ALMA beam. The dotted black line indicates the approximate direction of the nuclear bar (PA = 75°, see Fig. 17a), and the dashed lines are the kinematic major and minor axes (MKA and mKA). The small green contour at the center is the lowest H_2O448 contour in Fig. 4b. The yellow dotted curves indicate circles in the plane of the galaxy with radii r = 3″, 2″, 1.5″, 1″, and 0.5″. d–h) Position-velocity diagrams along the above circles. The green curves show the purely rotational velocity field fitted by Pereira-Santaella et al. (2016) to a region of 10″ in size that excludes the nuclear region, with V_{rot} = 250, 260, 280, 280, and 150 km s^{-1} in *panels d–h*, respectively. We have here modified this velocity field in the nuclear region, including azimuthal variations of the rotational and radial velocity components of the gas, as depicted with the red dashed curves, with values for V_{rot} and V_{rad} displayed in Figs. 16a–b. The PA of the stellar bar is indicated in cyan, and the PA of the MKA and mKA are indicated with long and short vertical arrows, respectively. The clockwise direction of rotation is indicated with arrows in *panels a* and *d*. *Panel f*: labels "inf" and "out" indicate regions with a radial velocity component negative (inflow) and positive (outflow), respectively, colored according to the velocity shift. Contour levels in *panels d–h* are 4.5, 9.0, 13.5, 19, 27, 54, and 108 mJy beam^{-1}.

lines and the far-IR and submm continuum, but can we trace the formation of such an extreme nuclear region from the observed kinematics at larger spatial scales? Pereira-Santaella et al. (2016) reported the CO 2−1 map observed with ALMA on spatial scales of 10″ and with a resolution similar to that of the H_2O448 observations, ≈0.25″, thus providing an ideal tool to search for hints of inflowing gas. Pereira-Santaella et al. (2016) fit the large-scale velocity field in ESO 320-G030 by excluding the nuclear region where complex CO profiles were found; here we focus on the CO 2−1 in this nuclear region.

4.1.1. The velocity field

Figures 15a–c show the CO color-coded maps of integrated intensity (moment 0, between −300 and +300 km s^{-1}), the velocity field (moment 1) and velocity dispersion (moment 2),

respectively. The dotted line in these panels indicates the approximate direction of the nuclear bar (PA = 75°), which is well traced by the VLT/NACO K-band image shown in Fig. 17a. The green contour at the center in Figs. 15a–c is the lowest (most extended) contour of the H_2O448 line in Fig. 4b, emphasizing the compactness of the core+disk nuclear structure probed by the H_2O line as compared with the large-scale CO emission. The yellow dotted curves depict circles in the plane of the galaxy with radii r = 3″, 2″, 1.5″, 1″, and 0.5″. PV diagrams along these circles are shown in panels d–h, where the green curves indicate the velocity field fitted by Pereira-Santaella et al. (2016), that is, a uniform rotational velocity with no radial component. It is clearly seen in panels d-g that, around the PA of the bar and mostly overshooting it (i.e., at lower PA, in the clockwise direction of rotation), the bulk of the gas shows significant departures from these ordered circular motions.

We have then modified this regular velocity field to account for the main kinematic departures from the green curves:

$$V_{\rm LOS} = V_{\rm rot}\,\cos(\theta-\theta_0)\,\sin i + V_{\rm rad}\,\sin(\theta-\theta_0)\,\sin i, \quad (7)$$

where θ, increasing in the clockwise (rotation) direction, measures the angular position in the plane of the galaxy, θ_0 = 133° is the position angle of the major kinematic axis (MKA), i = 43° is the inclination angle, $V_{\rm rot}$ is the rotational velocity, and $V_{\rm rad}$ is the radial component of the velocity. Equation (7) takes into account that the NE region is the far-side of the disk (Fig. 11; see also Fig. 9 in Cazzoli et al. 2014), and hence any inflowing component ($V_{\rm rad} < 0$) in that region ($\sin(\theta-\theta_0) > 0$) will be blueshifted (see Fig. 15f). Similarly, the SW region corresponds to the near side of the disk, and any inflow component here would be redshifted. The modified velocity field is displayed with dashed red curves in panels d-h, and the curves of $V_{\rm rot}$ and $V_{\rm rad}$ along these circles are shown in Figs. 16a–b.

The integrated intensity map in Fig. 15a shows relatively strong emission not only along the bar but also at lower PA, resulting in an elongated shape along the minor kinematic axis (mKA). This is the region where the velocity dispersion is above 60 km s^{-1} (panel c) and where the velocity field shows strong disturbances (panel b). Two trailing spiral arms at pitch angle of ≈90° arise from each side of the bar.

The overall kinematics shown in Figs. 15d–g clearly illustrate that the bulk of the gas in the NE region of the disk, ahead of the bar major axis in the forward (rotation) direction (0 < PA < 75°, i.e., at around the mKA), is blueshifted, and the gas on the opposite SW region of the disk (PA < −105°) is redshifted (as indicated in panel f). This effect is already seen at r = 3″ (700 pc), and becomes increasingly pronounced toward the center. If the gas in these regions remains in the plane of the galaxy, the observed velocity shifts are ascribed to an inflow ($V_{\rm rad} < 0$), as $\cos(\theta-\theta_0) = 0$ along the mKA. In addition, we also find clear evidence of outflowing gas ($V_{\rm rad} > 0$) at PA higher than that of the bar (i.e., for gas that has not still arrived at the bar). The outflowing gas is clearly seen at PA ≈ −90° (see Fig. 15f); it is blueshifted (redshifted) on the western (eastern) side of the disk. Nevertheless, the magnitude of this velocity is significantly lower than the inflow velocity ahead of the bar, except at r = 3″ where both are similar (Fig. 16b).

Our fit to the PV diagrams in Figs. 15d–g, with results for $V_{\rm rot}$ and $V_{\rm rad}$ in Figs. 16a–b, respectively, is based on the observed slope and values of $V_{\rm LOS}$. Around the mKA, where gas on both sides of the disk shows inflowing velocities, $V_{\rm rad} < 0$ is well constrained from the values of $V_{\rm LOS}$. Inflow velocities as large as 80−180 km s^{-1} are obtained at r = 2″−1″ (460−230 pc). The slope of $V_{\rm LOS}$ in these PA regions indicates that, at r = 1″−2″, $V_{\rm rot}$ sharply decreases to 150−200 km s^{-1}. At PA around 105° and −75°, where outflowing gas is detected, we have some degeneracy between $V_{\rm rot}$ and $V_{\rm rad}$, which is approximately solved from the slope of $V_{\rm LOS}$. At r = 3″, we find some evidence of increasing $V_{\rm rot}$ at the trailing edge of the bar. At $r \le 1''$, the CO lines become very broad with FWZI of ≈400 km s^{-1}; the high turbulence masks both the rotation field and any possible inflow in these innermost regions, although hints of a velocity pattern similar to that found at higher r are seen on the NE side of the disk. The inflow in this region is better probed by the OH lines (Sect. 4.2).

Besides the above velocity field that applies to the bulk of gas at different radii and PA, Fig. 15 also shows a low intensity component that is fully decoupled from the overall pattern but is also symmetric relative to the center. It is traced by the lowest contour(s) in the velocity-position maps of panels e–g, showing very-high velocity dispersion. This component is already seen at r = 2″ around PA ≈ 30° and, symmetrically, around PA ≈ −150° (panel e), with line-of-sight velocities that extend from the velocity of the rotating gas at that position to a similar velocity but with opposite sign. As r decreases to 1″, the

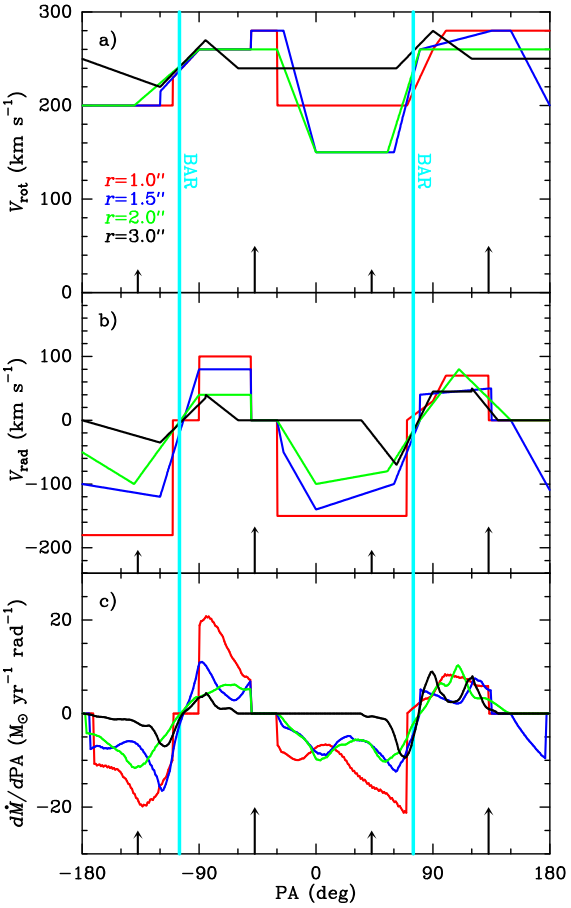

Fig. 16. (*a*) Rotational and (*b*) radial velocity components of the gas along the four outer circles (r = 1″ − 3″) depicted in Figs. 15a–c, as derived from the CO (2–1) PV diagrams of Figs. 15d–g. (*c*) The rate at which gas mass is crossing the quoted circles per unit interval of PA. The PA of the bar is indicated with cyan vertical lines, and the vertical long and short arrows indicate the PA of the MKA and mKA, respectively. Values of $V_{\rm rad}$ and $d\dot{M}/d$PA positive (negative) indicate gas flowing in the outward (inward) direction.

component becomes more extended in PA. The overall direction of this component is similar to that of the outflowing clumps observed in CO 2–1 (Pereira-Santaella et al. 2016), and to the direction of the bipolar outflow seen in NaD as well (Cazzoli et al. 2014). It is thus possible that this CO component represents the low-velocity counterpart of the CO outflow, with a relatively high opening angle that enables both negative and positive line-of-sight velocities at a given position. Nevertheless, a more plausible interpretation suggested by the limiting velocities and also by the location of this component ahead of the bar major axis, is that it represents the kinematic effect of the strong shock produced by the gas overshooting the bar. The fraction of gas mass sampled within a velocity range of $\pm 50\,\mathrm{km\,s^{-1}}$ around the red curves in Figs. 15d–g ranges from 43% at $r = 1''$ to 87% at $r = 3''$.

4.1.2. The gas flow

The Pa-α image in Fig. 17b (from Alonso-Herrero et al. 2006) shows ring-like emission with a radius of $\sim 4'' \sim 1$ kpc, at the expected location of the inner Lindblad resonance (ILR) of the primary bar where the gas tends to pile up and star formation is likely to proceed. Friedli & Martinet (1993) argued that, in order to avoid chaos around the principal resonances, a double-bar system evolves with the corotation radius $R_{\rm cor}$ of the nuclear bar coincident with the ILR of the large-scale bar (see also Hunt et al. 2008), and we indeed observe CO emission along the nuclear gas bar approaching the Pa-α ring (Fig. 17b). Using $R_{\rm cor} \sim (1.2{-}1.4) \times R_{\rm bar}$ (Athanassoula 1992), appropriate for fast rotating bars, also gives a similar $R_{\rm cor} \sim 1$ kpc. The nuclear bar pattern speed is expected to be $\Omega_s = V_{\rm rot}(R_{\rm cor})/R_{\rm cor} \sim 250\,\mathrm{km\,s^{-1}\,kpc^{-1}}$, where we have used the observed velocity field fitted by Pereira-Santaella et al. (2016). Such a high value of Ω_s indicates that the nuclear bar is decoupled from the primary bar; simulations indeed indicate that the decoupling requires both the presence of the primary bar ILR and the anti-bar x_2 orbit family (Friedli & Martinet 1993). The properties of the nuclear bar of ESO 320-G030 (length and Ω_s) are similar to those of NGC 2782 (Hunt et al. 2008). At $r = 1'' - 3''$ (230–700 pc), the velocity of the bar is $60{-}180\,\mathrm{km\,s^{-1}}$. Therefore, the gas on the trailing edge outruns the bar, but the gas on the leading edge has a small rotational velocity ($50{-}150\,\mathrm{km\,s^{-1}}$) in the frame of the rotating bar, comparable to or even lower than the inflow velocities in the same region.

The K-band image of ESO 320-G030, displayed in Fig. 17a, probes the nuclear bar rather well, with still a V-shaped apparent absorption at PA $= 20°{-}60°$ probably caused by the outflow observed around that direction (Pereira-Santaella et al. 2016; Cazzoli et al. 2014). The velocity vectors of the molecular gas along the $r = 1''{-}3''$ circles, projected on the plane of sky, are overlaid on this image. Most of the CO emission along the gas bar is spatially shifted in the clockwise (rotation) direction relative to the stellar bar. The inflowing gas ($V_{\rm rad} < 0$) is also seen ahead of the bar major axis, and the outflowing gas is observed on the opposite sides, so that both mark the intersections of the gas flow, which is elongated along the bar, with the circles. Nevertheless, owing to the asymmetry of the negative and positive values of $V_{\rm rad}$ (Fig. 16b), the lines of gas flow are not expected to be closed, but will spiral onto the nuclear region.

Since the gas orbits are expected to be approximately stationary in the rotating bar frame, we show in Fig. 18 the deprojected images of CO 2–1 and 454 GHz continuum, together with the inferred velocity vectors in the frame of the bar after correcting for the assumed $\Omega_s = 250\,\mathrm{km\,s^{-1}\,kpc^{-1}}$. The whole image is rotated such that the bar lies in the horizontal direction. In this frame, the velocity vectors are nearly parallel to the isocontours of CO emission at the leading edge of the gas bar, and are perpendicular to the bar where the gas crosses it. Therefore, our inferred velocity field approximately accounts for the morphology of the leading edge of the gas bar, where the gas flows parallel to the bar and in the inward direction. This point is better seen with the two green curves of Fig. 18, which are generated by integrating over time the velocity vector. The departing points are selected so as the lines get close to the $3''$ circle when crossing the bar. The curves should be considered with caution, as the velocity field is only determined at four radial positions and a linear interpolation is performed at all other radii. Nevertheless, they seem to delineate rather well the leading edge of the CO gas bar. This connection between kinematics and morphology gives support to the model, and illustrates the very efficient bar mechanism to drive a massive inflow. While these green lines cannot be considered realistic gas "orbits," due to complex events such as shocks at the bar position, they represent prominent (dominant) lines of gas flow associated with the velocity component in red in Figs. 15d–g, and as such they have an associated timescale. The elapsed time along the calculated lines is 13 and 24 Myr, corresponding to $\sim 0.5{-}1$ turns of the bar.

4.1.3. The mass inflow rate

We estimate the instantaneous mass inflow rate at a radius r as the net gas mass crossing in the inward direction the circles depicted in Figs. 15a–c per unit time:

$$\dot{M}_{\rm inf}(r) = -\oint {\rm d}l_c \, \frac{{\rm d}M_{\rm rad}}{{\rm d}l_c} \, \frac{V_{\rm rad}}{\Delta r_B} = -\frac{\alpha_{\rm CO}\, r}{A_{\rm B}} \int_0^{2\pi} {\rm d}\theta \, L'_{\rm CO}(r,\theta)\, V_{\rm rad}(r,\theta)\, f_{\rm r}(\theta)\, f_{\rm s}(\theta), \quad (8)$$

where ${\rm d}l_c$ is an arc element in the plane of the galaxy, ${\rm d}M_{\rm rad}$ measures the gas mass with $V_{\rm rad} \neq 0$, $A_{\rm B}$ is the beam area at the source distance, and $\Delta r_{\rm B} = A_{\rm B}^{1/2}/f_{\rm r}$ is the radial interval sampled by the beam in the galaxy plane. This equation integrates over the circles the gas mass flowing with $V_{\rm rad} \neq 0$ divided by $\Delta t = \Delta r_{\rm B}/V_{\rm rad}$, where $V_{\rm rad}$ is displayed in Fig. 16b. In the second equality of Eq. (8), the CO luminosity $L'_{\rm CO}$ only involves line-of-sight velocities within $\pm 50\,\mathrm{km\,s^{-1}}$ from the red curves in Figs. 15d–g. We adopt a conversion factor $\alpha_{\rm CO} = 0.78\,M_\odot/(\mathrm{K\,km\,s^{-1}\,pc^2})$, and implicitly assume the same brightness for the CO 1–0 and 2–1 lines. Finally, $f_{\rm r}$ and $f_{\rm s}$ (both within the range 0.73–1) are geometrical factors that account for the source inclination; $f_{\rm r}$ corrects for the radial interval sampled by the beam on the plane of the source, and $f_{\rm s}$ corrects for the projection of the circular arcs on the plane of the sky:

$$f_{\rm r} = \left[\cos^2(\theta - \theta_0) + \sin^2(\theta - \theta_0)\cos^2 i\right]^{1/2}$$
$$f_{\rm s} = \left[\sin^2(\theta - \theta_0) + \cos^2(\theta - \theta_0)\cos^2 i\right]^{1/2} \quad (9)$$

Equation (8) implicitely corrects the gas mass crossing the circles in the inward direction ($V_{\rm rad} < 0$) for that crossing them in the outward direction ($V_{\rm rad} > 0$), and can be thus considered net inflow rates. The values of ${\rm d}\dot{M}/{\rm dPA}$ as a function of PA are displayed in Fig. 16c, where negative (positive) values indicate inflowing (outflowing) contributions. It shows that the outflowing mass does not cancel the inflowing mass at $r \leq 2''$, although a massive outflowing clump is seen at PA $\approx -90°$ for $r = 1''$.

The values of $\dot{M}_{\rm inf}$ are listed in Table 3. At $r = 1.5''{-}1''$, $\dot{M}_{\rm inf} = 16 - 20\,M_\odot\,\mathrm{yr^{-1}}$ is similar to our estimated nuclear

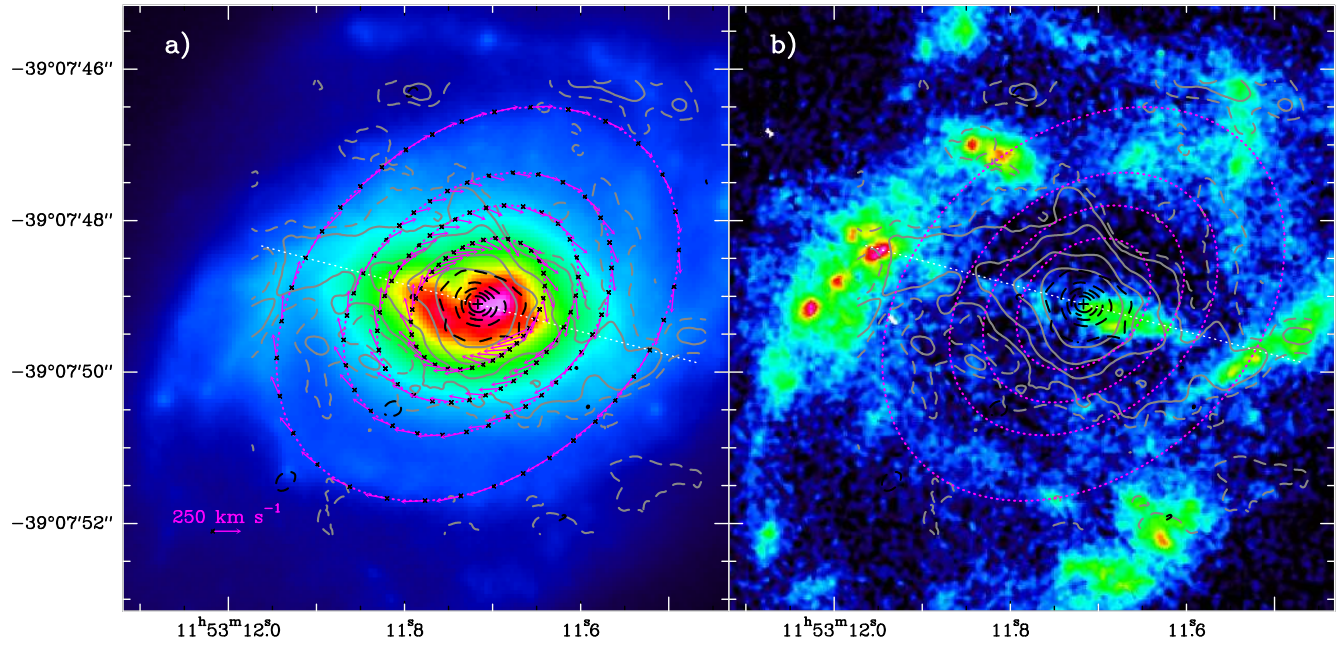

Fig. 17. Images of the central region of ESO 320-G030 in VLT/NACO *K*-band (Crespo Gómez et al., in prep.; *panel a*) and in the HST/NICMOS2 F190N-F187N (continuum-subtracted Pa-α, from Alonso-Herrero et al. 2006, reprocessed using the latest NICMOS pipeline by Sánchez-García et al. in prep.; *panel b*). The CO (2–1) emission observed with ALMA (gray contours) and the 454 GHz continuum (dashed black contours) are overlaid in both panels. The direction of the nuclear gas bar is indicated by the dotted white line (PA = 75°). The four outer circles of Figs. 15a–c (r = 1″–3″) where the velocity field is estimated are also indicated, with the arrows in panel a showing the gas velocity vectors projected on the plane of sky. The cross marks the position of the peak emission in CO, H_2O448, and 454 GHz continuum. For consistency with the ALMA astrometry, the VLT and HST images were aligned to the *Gaia* catalog using several stars in the field. The spatial resolutions are ∼0.25″ and ∼0.15″ for the VLT/NACO and HST/NICMOS images, respectively.

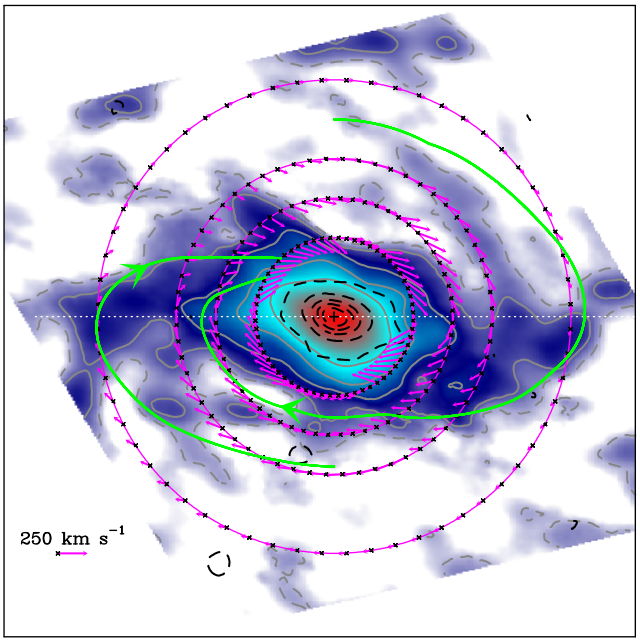

Fig. 18. Deprojected images of the CO 2−1 emission (colored scale and gray contours) and of the 454 GHz continuum (dashed black contours), which have been also rotated to have the bar (dotted white line) horizontal. The magenta arrows show the inferred velocity vectors along the r = 1″–3″ circles in the frame of the rotating bar, after correcting for an assumed nuclear bar pattern speed of Ω_s = 250 km s^{-1} kpc^{-1}. The green lines are the result of integrating the velocity vector in this rotating frame (with linear radial interpolation of the velocity field), with departing points at ±90° from the bar and r = 1.9″–2.5″, up to the point where they intersect the r = 1″ circle.

SFR (∼16–18 $M_\odot$ yr^{-1}, Sect. 3.2.3), strongly suggesting that the nuclear starburst is fed and sustained by the observed inflow. Our $\dot{M}_{\rm inf}$ values are not corrected by the feedback from the nuclear region, although $\dot{M}_{\rm outf} < 10\,M_\odot$ yr^{-1} (Pereira-Santaella et al. 2016). We have also estimated in Table 3 the inward flux of angular momentum across the quoted circles, by including the factor $r\,V_{\rm rot}(r,\theta)$ in the second equality of Eq. (8). While $\dot{L}_{\rm inf}$ is negative at r = 3″, meaning a net transfer of angular momentum outward, its value at shorter radii does not show a clear dependence on r.

The timescale associated with the inflow is $t \sim M_{\rm gas}/\dot{M}_{\rm inf}$, where $M_{\rm gas}$ is the gas mass of the nuclear region ($4.5\times10^8\,M_\odot$, Sect. 3.2.5). This gives the time for complete nuclear gas replenishment, $t \sim 23$ Myr, which corresponds to ∼ 1 rotation period of the nuclear bar. This timescale is similar to the elapsed time estimated for the longest curve in Fig. 18, $t \sim 24$ Myr. Since the gas mass enclosed in the annulus between r = 1″ and r = 3″ is $3.6\times10^8\,M_\odot$ (Sect. 3.2.5), it gives an independent estimate of $\dot{M}_{\rm inf} \sim 15\,M_\odot$ yr^{-1}. The similarity of both estimates is encouraging, given that the former gives an "instantaneous" value (i.e., averaged over the time the flow crosses a radial distance equivalent to the beam size, ∼0.6 Myr at 100 km s^{-1}) while the latter is a value averaged over the next ∼20 Myr.

Our timescale for complete nuclear gas replenishment is also similar – to within a factor of 2– to the equivalent timescales estimated for NGC 4418 (González-Alfonso et al. 2012; Sakamoto et al. 2013) and Arp 299a (Falstad et al. 2017), two LIRGs with luminosities similar to ESO 320-G030 and showing also inflowing molecular gas toward their nuclei. It is also consistent with the expectedly short timescales of low-luminosity AGN duty cycles (García-Burillo & Combes 2012).

Table 3. Estimated mass inflow rates and inward fluxes of angular momentum across the four outer circles ($r = 1''-3''$) depicted in Figs. 15a–c.

r ($''$)	$\dot{M}_{\rm inf}$ [(a)] ($M_\odot\,{\rm yr}^{-1}$)	$\dot{L}_{\rm inf}$ [(a)] ($M_\odot\,{\rm pc\,km\,s^{-1}\,yr^{-1}}$)
3	∼0	-10^5
2	11.3	6.2×10^5
1.5	16.0	8.3×10^5
1	19.9	6.8×10^5

Notes. [(a)]Both $\dot{M}_{\rm inf}$ and $\dot{L}_{\rm inf}$ are net values.

4.1.4. The overall scenario

The kinematic model derived from the CO 2−1 data cube indicates an efficient mechanism that drives a massive inflow along the bar. The gas in the arms, which is rotating faster than the bar, overruns it with perpendicular incidence. At and beyond the leading edge of the bar, a negative torque is exerted by the stars that drains angular momentum of the molecular gas (García-Burillo et al. 2005; Hunt et al. 2008), generating orbits of high eccentricity that make the gas flow couple to the bar morphology. The steep change in the direction of the velocity vectors at the leading edge of the bar suggests the presence of a nearly radial shock front, which is offset from the bar major axis in the forward (rotation) direction (Kormendy & Kennicutt 2004). The gas approaching the bar in the perpendicular direction will shock the gas flowing parallel to the bar along its leading edge, coming from larger r. Dissipation of kinetic energy through these shocks and viscosity contribute to drive a quasi-radial inflow in the rotating bar frame; we expect that after just two crossings of the bar, the inflowing gas will accumulate, through a shock that drives turbulence, around the envelope and nuclear disk, thus feeding the nuclear starburst. In ESO 320-G030, the inflowing gas does not stall in a ring at the ILR of the nuclear bar, but continues all the way toward the inner ∼150 pc as evidenced by the high concentration of warm molecular gas forming the structures probed by H_2O and other species (Appendix A). The enhanced nuclear star formation as derived from the IR luminosities of the nuclear disk and envelope (Sect. 3.2.3) strongly suggests that we are viewing a pseudobulge in formation, namely, a proto-pseudobulge.

We obtain inflow velocities comparable in magnitude to those inferred in NGC 1530 (Regan et al. 1997), and also increasing toward the center. With decreasing distance to the nucleus, shocks increase the gas turbulence and the inflow becomes more disordered and not restricted to the plane of the galaxy. Figure 15c shows that velocity dispersion as measured by CO 2–1 apparently decreases just at the nucleus. This decreasing ΔV is associated with a nuclear blue asymmetric self-absorbed CO profile (Pereira-Santaella et al. 2017), illustrating that the inflowing gas from the SW region is also seen in front of the nucleus at small radii. The increasing flow distortion, with gas inflowing along orbits not contained in the galaxy plane, is also required to account for the redshifted velocities found in the OH 119 and 79 μm doublets observed in absorption (Sect. 4.2), indicating the presence of gas with line-of-sight velocities of $\sim100\,{\rm km\,s^{-1}}$. It is plausible that this represents the effect of vertical resonances on the gas flow that make the inflow 3D (Pfenniger & Norman 1990). The extra-planar flow of gas may also have a contribution from the fountain effect generated by the neutral outflow (Cazzoli et al. 2014), which remains gravitationally bound to the galaxy.

4.2. The inflow observed in the far-IR

Clear evidence of inflowing gas is also seen in the far-IR. The [O I] 63 μm line shows a blue asymmetric profile with redshifted absorption at $\approx100\,{\rm km\,s^{-1}}$ (Fig. 20a). Unlike the case of NGC 4418 (González-Alfonso et al. 2012), however, the redshifted part of the profile is seen in emission above the continuum, probably because the continuum emission from ESO 320-G030 is less spatially concentrated than in NGC 4418.

The observed OH doublets, indicated in the energy level diagram of Fig. 19, show a sequence in the velocity of the absorption as a function of the lower level energy and line optical depth (Figs. 20b–g): The ground-state and optically thick OH 119 μm doublet peaks at $\approx100\,{\rm km\,s^{-1}}$; the cross-ladder ground-state OH 79 μm doublet, with lower opacity, also shows evidence for redshifted absorption but at lower velocities; the OH 84 μm doublet, with $E_{\rm lower} = 120$ K, still shows some hints of redshifted absorption, but the high-lying OH 65 and 71 μm doublets, with $E_{\rm lower} = 290$ and 415 K, respectively, peak at central velocities. Since the doublets progressively probe more excited (and therefore more central) regions, the inflow dissipates its kinetic energy when approaching the very inner regions of the nucleus (i.e., the disk, where inflow motions are still seen, and the core).

On the other hand, the high OH column densities (see below) required to account for the observed absorption suggest that these are produced within the nuclear region sampled by H_2O. Therefore, we explore here whether the inflow observed in the far-IR is primarily associated with the outermost nuclear H_2O component, that is, the envelope, responsible for the low-lying H_2O far-IR absorption and submm emission lines. Indeed, hints of redshifted absorption are also seen in the H_2O138 and H_2O75 lines (Fig. 8). This inflowing region is smaller ($r \lesssim 0.5''$, Fig. 11) than that sampled by CO ($1''-2''$, Fig. 15).

We have then applied the composite H_2O fiducial model to OH, but have included a velocity field as follows: For the envelope, the gas is inflowing with a velocity of $100\,{\rm km\,s^{-1}}$ at the outermost radius and decreasing linearly with radius; for the disk, an inflow velocity of $60\,{\rm km\,s^{-1}}$ is adopted. No velocity field is included for the core component. Model results are overlaid on the observed line profiles in Figs. 20b–e, and are roughly consistent with the scenario that the inverse P-Cygni OH 119 μm and 79 μm profiles are driven by an inflow within the envelope that primarily applies to the external shells (110−150 pc). Since this component is optically thin in the far-IR continuum, it generates inverse P-Cygni profiles in OH 119 and OH 84 μm but a blue asymmetric profile in OH 79 μm (gray dashed curves in Fig. 20). Toward the optically thick disk and core components all doublets are predicted in absorption, and the blue asymmetric profile of the OH 163 μm doublet is produced by the redshifted absorption toward the disk (green dashed curve in Fig. 20d). The net modeled profiles (shown in red) resemble the observed ones although with significant discrepancies in the OH 119 μm doublet.

The OH column density of the inflowing gas in the envelope is $N_{\rm OH} = 3.2\times10^{16}\,{\rm cm^{-2}}$. To estimate the associated mass inflow rate, we adopt a geometry consisting of two shells on opposite sides, each with radius $R \sim 130$ pc, surface πR^2, and width $\Delta R \sim 40$ pc, inflowing with an average velocity of $V_{\rm inf} \sim 80\,{\rm km\,s^{-1}}$, so that

$$\dot{M}_{\rm inf} \sim \frac{2\,N_{\rm OH}\,\mu\,m_{\rm H}\,\pi R^2\,V_{\rm inf}}{X_{\rm OH}\,\Delta R}, \quad (10)$$

which results in $\dot{M}_{\rm inf} \sim 30\,M_\odot\,{\rm yr^{-1}}$ for a fiducial OH abundance of $X_{\rm OH} \sim 2.5\times10^{-6}$. While this estimate is admittedly rather uncertain, it is consistent with the scenario of several dozens solar masses per year of gas feeding the nucleus of ESO 320-G030, as inferred from CO.

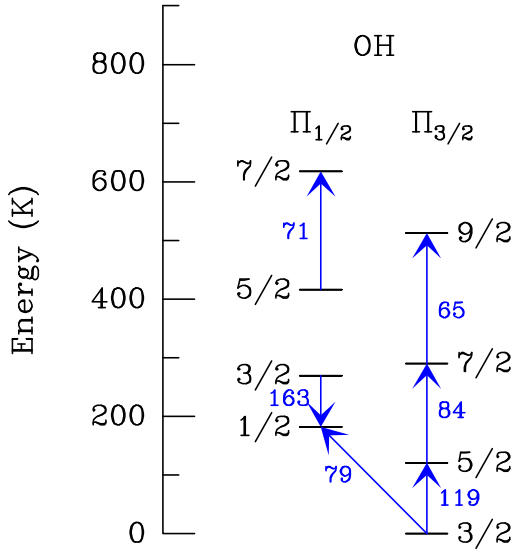

Fig. 19. Energy level diagram of OH indicating the lines observed with *Herschel*/PACS (blue arrows and labels). Labels denote the rounded wavelengths in μm. Upward (downward) arrows indicate lines detected primarily in absorption (emission).

5. Discussion and conclusions

The combined analysis of the H_2O absorption and emission lines in ESO 320-G030, with wavelengths ranging from 58 to 669 μm, and the continuum, together with high-resolution data obtained with ALMA for the H_2O448 line and the associated submm dust emission, unveils the structure of the galactic nucleus which we suggest is evidence for the presence of a prominent proto-pseudobulge fed by a molecular inflow driven by a strong nuclear bar. The radius of the most extended region of the nucleus (the envelope component, ~200 pc) is in the lower range of measured pseudobulge sizes (e.g., Carollo 1999; Fisher & Drory 2008). The radius will likely increase in view of the CO gas reservoir around the nucleus, with a mass comparable to that of the nucleus. Our 3D model for the H_2O448 line shape indicates a velocity field with $V_{\rm rot}/\sigma \sim 1$, meaning that there is an increase in random motions relative to ordered gas motions in the nuclear disk. Stellar kinematics indicate a value of $V_{\rm rot}/\sigma \sim 0.7$ within an aperture of $r = 150$ pc, also showing an increase in random motions in the nuclear region while retaining a memory of the rotation (A. Crespo Gómez et al., in prep.).

The envelope has typical columns of several $\times 10^{23}$ cm^{-2} and is moderately warm ($T_{\rm dust} \approx 50$ K). With these conditions, the low-lying H_2O lines at submm wavelengths (240–400 μm) are efficiently pumped, but little absorption is produced in the far-IR with only significant absorption in the H_2O lines at 75 and 108 μm. Nevertheless, the inferred colums are more than enough to extinguish any line emission at short wavelengths, and indeed the Pa-α emission within $r = 0.5$ kpc primarily probes the western (near) side of the nuclear bar, with a morphology different from that of the continuum submm emission (Fig. 17b). It is within the envelope region where the CO 2–1 line becomes very broad (Fig. 15c), which is probably a direct consequence of the shocks produced by the inflowing gas and may be evidence of disordered motions that would eventually lead to a pseudobulge.

High-lying molecular absorption lines in the far-IR are produced when the columns are so high that the far-IR continuum becomes optically thick (González-Alfonso et al. 2015), and these conditions are also linked to the emission in the H_2O448 line. In ESO 320-G030, a nuclear disk with projected radius

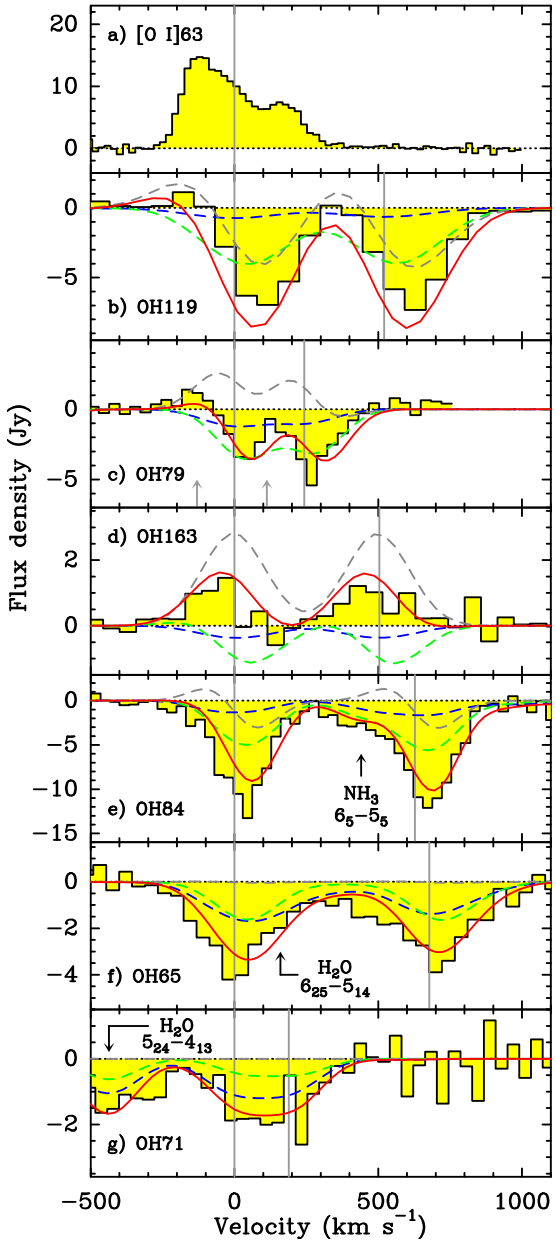

Fig. 20. Inflow in ESO 320-G030 observed in the far-IR [O I] 63 μm line and OH doublets. The gray vertical lines indicate the position of the two components of the OH doublets (blended within a single feature in the case of OH 71 μm in *panel g*), and the vertical arrows in panel c indicate the position of the ^{18}OH 79 μm doublet components. OH is modeled with the same components as derived from H_2O: the core (dashed blue lines), the nuclear disk (dashed green) and the envelope (dashed gray); red is total. The inflow is simulated in the envelope component (see Sect. 4.2). The model also includes the contribution by ^{18}OH, NH_3, and H_2O in *panels c, e, and f–g*, respectively (see Appendix A).

of ≈40 pc attains these conditions, though still with moderately warm dust ($T_{\rm dust} \approx 55$ K). The disk is distorted, elongated in the direction of the bar, and highly turbulent ($\Delta V/V_{\rm rot} \approx 1$); it is thus expected to be geometrically thick (e.g., Cazzoli et al. 2020).

At the center of the disk, an unresolved, extremely buried ($\tau_{100} \gg 1$) and very warm ($T_{\rm dust} \sim 100$ K for the far-IR photosphere; see González-Alfonso & Sakamoto 2019) core component is identified from the absorption detected in very high-lying lines of H_2O, of which the $H_2O\,7_{07}-6_{16}$ line at 71.95 μm ($E_{\rm lower} = 640$ K) is an excellent tracer. We estimate

a core radius of $R = 9-16$ pc, but higher angular resolution observations are required to better determine its size. HCN vibrational emission has been recently detected in ESO 320-G030 (Falstad et al., in prep.), additionally indicating the presence of a very warm optically thick region. In such environments, trapping of IR radiation raises $T_{\rm dust}$ and the mid-IR radiation density within the cocoon of dust, but the resulting SED does not show any enhanced mid-IR emission as only the photosphere is probed at mid- and even far-IR wavelengths (González-Alfonso & Sakamoto 2019). Because of their extreme extinction, the nature of these very compact nuclear components has been long debated; even X-rays and mid-IR high ionization tracers from a putative AGN are expected to be severely attenuated. ESO 320-G030 is undetected with the *Swift*/BAT all-sky survey observations[1] in the 14−195 keV band with a sensitivity of 8.4×10^{-12} erg s^{-1} cm^{-2}, which translates into a luminosity of $<6 \times 10^8\,L_\odot$. Assuming a ∼5% contribution to the bolometric AGN luminosity in the quoted band, the upper limit for $L_{\rm AGN}$ is $\lesssim 10^{10}\,L_\odot$; however, absorption at <30 keV is still relevant for $N_{\rm H} \sim 10^{25}$ cm^{-2}, and an AGN with ∼10% of the total galaxy luminosity is still possible. Assuming this limiting AGN scenario, a mass accretion rate onto the black hole of BHAR $\sim 0.01\,M_\odot$ yr^{-1} would be required for a fiducial radiative efficiency of 0.1. This BHAR is a factor of $\sim 6 \times 10^{-4}$ times the estimated nuclear SFR, matching the volume-averaged BHAR/SFR ratio in local bulge-dominated galaxies (Heckman et al. 2004). Using $M_{\rm dyn} \approx 2 \times 10^9\,M_\odot$ for $r < r_{\rm H_2O}$ (Sect. 3.2.5) as a proxy for the mass of the pseudobulge in formation, and the $M_{\rm BH}/M_{\rm bulge} \sim 2.5 \times 10^{-3}$ ratio appropriate for small bulges (Kormendy & Ho 2013), the resulting $M_{\rm BH} \sim 5 \times 10^6\,M_\odot$[2] would be emitting at a high level of 0.1 $L_{\rm Edd}$. This very crude estimate is comparable to the high Eddington ratio (∼0.3) estimated for NGC 4418 if an AGN is assumed to power its compact nucleus (Sakamoto et al. 2013).

The nuclear core may still be primarily powered by a starburst, with a limiting luminosity surface density of $\sigma\,T_{\rm dust}^4 \sim 10^{13}\,L_\odot$ kpc^{-2}. This is close to the value theoretically expected for radiation-pressure supported starburst disks (Thompson et al. 2005). Even in this scenario, the core component is expected to host a growing SMBH at the center of the galaxy, given the nuclear feeding reservoir ($M_{\rm gas} \sim 10^8\,M_\odot$ within ∼12 pc) and excellent conditions for such fast growth (probably constrained by radiation pressure on dust grains). Statistically, Seyfert galaxies are preferentially found in barred systems (e.g., Maia et al. 2003).

Excluding the luminosity of the core component, the averaged nuclear SFR surface density is $\log \Sigma_{\rm SFR}$ ($M_\odot$ yr^{-1} kpc^{-2}) ∼ 2.1, and the averaged nuclear molecular gas surface density is $\log \Sigma_{\rm H2}$ ($M_\odot$ pc^{-2}) ∼ 3.6. Thus the nuclear region of ESO 320-G030 lies near the high end of the Schmidt law for starburst galaxies (Kennicutt 1998).

Bars within bars were long ago understood to provide an efficient way to drive gas toward the very inner centers of galaxies (e.g., Shlosman et al. 1989), and ESO 320-G030 appears to be a prototypical example of such a system. The nuclear region is moderately elongated along the bar as traced primarily by the dust continuum image at 454 GHz, and a massive inflow is found in the inner ≈0.5 kpc of the galaxy from the analysis of the CO 2–1 data cube. The azimuthal velocity of the molecular gas sharply decreases across the bar, resembling the large velocity jumps observed across optical dust lanes associated with bars (e.g., Regan et al. 1997). The molecular inflow, with typical radial velocities of 80−150 km s^{-1}, is indeed strongly associated with the nuclear bar. Two independent estimates of the mass inflow rate from CO yield similar values, $\dot{M}_{\rm inf} \sim 15-20\,M_\odot$ yr^{-1}. Since these values are similar to the SFR of the nuclear region ($16-18\,M_\odot$ yr^{-1}), we conclude that the enhanced nuclear starburst is fed and sustained by the observed inflow. These inflow velocities are also observed in the ground-state OH doublets at 119 and 79 μm as redshifted absorption, probing line-of-sight velocities toward the source of far-IR continuum that indicate a complex 3D flow not restricted to the plane of the galaxy. The inflowing gas probed by OH appears to be more compact than that sampled by CO; it is associated with the envelope component and its kinetic energy dissipates at spatial scales of the nuclear disk (<100 pc). The mass inflow rate inferred from OH is $\sim 30\,M_\odot$ yr^{-1}, comparable to that derived from CO.

The timescale associated with the inflow, ∼20 Myr, is also expected to characterize the timescale over which the current nuclear burst will fade, once the gas reservoir within the ILR of the primary bar is fully accreted onto the nucleus. This is at least one order of magnitude shorter than typical formation timescales of pseudobulges as inferred for circumnuclear star-forming rings in barred galaxies (Kormendy & Kennicutt 2004), indicating that atypically short timescale secular evolution, extreme accumulations of gas, and plausibly fast growing SMBHs may characterize nuclei of galaxies with strong nuclear bars.

While the case of ESO 320-G030 is exceptional in the local universe, how common are these nuclear gas concentrations at $z > 1$, when the cosmic accretion rate required to sustain the observed SFR in massive main sequence galaxies was $\gtrsim 15\,M_\odot$ yr^{-1} (Scoville et al. 2017), similar to the value we obtain for the nuclear region of ESO 320-G030? How does that matter accrete onto galaxies, and how is it redistributed? What is the impact of short-range, intense bursts of nuclear star formation on overall galaxy evolution over cosmic time? Far-IR spectroscopy provides a unique way of measuring the spatial structure of star formation during prolific stages of nuclear gas accumulation, which can be unveiled with future far-IR facilities similar to the recently cancelled SPace Infrared telescope for Cosmology and Astrophysics (SPICA) (Roelfsema et al. 2018)[3].

Acknowledgements. EG-A is grateful for the warm hospitality of the Harvard-Smithsonian Center for Astrophysics, where part of the present study was carried out, and thanks Javier Goicoechea for useful conversations on the far-IR spectrum of Sgr B2, Alex Crespo Gómez for sharing preliminary results on the stellar kinematics in ESO 320-G030, and Juan Rafael Martínez-Galarza for useful conversations on the Bayesian analysis. We thank the anonymous referee for constructive and helpful comments on the manuscript. PACS was developed by a consortium of institutes led by MPE (Germany) and including UVIE (Austria); KU Leuven, CSL, IMEC (Belgium); CEA, LAM (France); MPIA (Germany); INAFIFSI/OAA/OAP/OAT, LENS, SISSA (Italy); IAC (Spain). This development has been supported by the funding agencies BMVIT (Austria), ESA-PRODEX (Belgium), CEA/CNES (France), DLR (Germany), ASI/INAF (Italy), and CICYT/MCYT (Spain). SPIRE was developed by a consortium of institutes led by Cardiff University (UK) and including Univ. Lethbridge (Canada); NAOC (China); CEA, LAM (France); IFSI, Univ. Padua (Italy); IAC (Spain); Stockholm Observatory (Sweden); Imperial College London, RAL, UCL-MSSL, UKATC, Univ. Sussex (UK); and Caltech, JPL, NHSC, Univ.Colorado (USA). This development has been supported by national funding agencies: CSA (Canada); NAOC (China); CEA, CNES, CNRS (France); ASI (Italy); MCINN (Spain); SNSB (Sweden); STFC, UKSA (UK); and NASA (USA). This paper makes use of the following ALMA data: ADS/JAO.ALMA#2016.1.00263.S and

[1] https://swift.gsfc.nasa.gov/results/bs105mon/

[2] Using the observed $\Delta V \approx 100$ km s^{-1} as a proxy for the stellar velocity dispersion that would result once the gas is locked onto stars, and the observed $M_{\rm BH}/\sigma$ correlation by Tremaine et al. (2002), a slightly higher $M_{\rm BH} \sim 8 \times 10^6\,M_\odot$ is obtained.

[3] During the final stages of preparation of this manuscript, the SPICA mission was cancelled by ESA prior to the scheduled Mission Selection Review; see Clements et al. (2020) and https://spicarebelalliance.com.

ADS/JAO.ALMA#2013.1.00271.S. ALMA is a partnership of ESO (representing its member states), NSF (USA) and NINS (Japan), together with NRC (Canada) and NSC and ASIAA (Taiwan) and KASI (Republic of Korea), in cooperation with the Republic of Chile. The Joint ALMA Observatory is operated by ESO, AUI/NRAO and NAOJ. Based on observations made with ESO Telescopes at the Paranal Observatory under programme ID 086.B-0901(A). EG-A is a Research Associate at the Harvard-Smithsonian Center for Astrophysics. EG-A, JM-P, and FR-V thank the Spanish Ministerio de Economía y Competitividad for support under projects ESP2017-86582-C4-1-R and PID2019-105552RB-C41. EG-A and HAS thank NASA grant ADAP NNX15AE56G. MP-S acknowledges support from the Comunidad de Madrid, Spain, through Atracción de Talento Investigador Grant 2018-T1/TIC-11035 and PID2019-105423GA-I00 (MCIU/AEI/FEDER,UE). AA-H and SG-B acknowledge support through grant PGC2018-094671-B-I00 (MCIU/AEI/FEDER,UE). LC, AA-H, MP-S, and JM-P acknowledge support under project No. MDM-2017-0737 Unidad de Excelencia "María de Maeztu" – Centro de Astrobiología (INTA-CSIC). SG-B acknowledges support from the Spanish MINECO and FEDER funding grant AYA2016-76682-C3-2-P. C.Y. acknowledges support from an ESO Fellowship. LC acknowledges support from the Spanish Ministerio de Economía y Competitividad for support under project ESP2017-83197. SC acknowledges financial support from the State Agency for Research of the Spanish MCIU through the 'Center of Excellence Severo Ochoa' award to the Instituto de Astrofísica de Andalucía (SEV-2017-0709). This research has made use of NASA's Astrophysics Data System (ADS) and of GILDAS software (http://www.iram.fr/IRAMFR/GILDAS).

References

Aalto, S., Martín, S., Costagliola, F., et al. 2015, A&A, 584, A42
Aladro, R., König, S., Aalto, S., et al. 2018, A&A, 617, A20
Alonso-Herrero, A., Rieke, G. H., Rieke, M. J., et al. 2006, ApJ, 650, 835
Alonso-Herrero, A., Pereira-Santaella, M., Rieke, G. H., & Rigopoulou, D. 2012, ApJ, 744, 2
Arribas, S., Colina, L., Monreal-Ibero, A., et al. 2008, A&A, 479, 687
Arribas, S., Colina, L., Bellocchi, E., Maiolino, R., & Villar-Martín, M. 2014, A&A, 568, A14
Athanassoula, E. 1992, MNRAS, 259, 345
Baan, W. A., & Klöckner, H. R. 2006, A&A, 449, 559
Bellocchi, E., Arribas, S., Colina, L., & Miralles-Caballero, D. 2013, A&A, 557, A59
Bellocchi, E., Arribas, S., & Colina, L. 2016, A&A, 591, A85
Briggs, D. S. 1995, Am. Astron. Soc. Meeting Abstracts, 187, 112.02
Carollo, C. M. 1999, ApJ, 523, 566
Cazzoli, S., Arribas, S., Colina, L., et al. 2014, A&A, 569, A14
Cazzoli, S., Arribas, S., Maiolino, R., & Colina, L. 2016, A&A, 590, A125
Cazzoli, S., Gil de Paz, A., Márquez, I., et al. 2020, MNRAS, 493, 3656
Cernicharo, J., Goicoechea, J. R., & Caux, E. 2000, ApJ, 534, L199
Clements, D. L., Serjeant, S., & Jin, S. 2020, Nature, 587, 548
Combes, F., & Sanders, R. H. 1981, A&A, 96, 164
Falstad, N., González-Alfonso, E., Aalto, S., et al. 2015, A&A, 580, A52
Falstad, N., González-Alfonso, E., Aalto, S., & Fischer, J. 2017, A&A, 597, A105
Fischer, J., Sturm, E., González-Alfonso, E., et al. 2010, A&A, 518, L41
Fischer, J., Abel, N. P., González-Alfonso, E., et al. 2014, ApJ, 795, 117
Fisher, D. B., & Drory, N. 2008, AJ, 136, 773
Franx, M., & de Zeeuw, T. 1992, ApJ, 392, L47
Friedli, D., & Martinet, L. 1993, A&A, 277, 27
García-Burillo, S., Combes, F., Schinnerer, E., Boone, F., & Hunt, L. K. 2005, A&A, 441, 1011
García-Burillo, S., Combes, F., Ramos Almeida, C., et al. 2019, A&A, 632, A61
García-Burillo, S., & Combes, F. 2012, J. Phys. Conf. Ser., 372, 012050
Goicoechea, J. R., Rodríguez-Fernández, N. J., & Cernicharo, J. 2004, ApJ, 600, 214
González-Alfonso, E., & Sakamoto, K. 2019, ApJ, 882, 153
González-Alfonso, E., Smith, H. A., Ashby, M. L. N., et al. 2008, ApJ, 675, 303
González-Alfonso, E., Fischer, J., Isaak, K., et al. 2010, A&A, 518, L43
González-Alfonso, E., Fischer, J., Graciá-Carpio, J., et al. 2012, A&A, 541, A4
González-Alfonso, E., Fischer, J., Bruderer, S., et al. 2013, A&A, 550, A25
González-Alfonso, E., Fischer, J., Aalto, S., & Falstad, N. 2014a, A&A, 567, A91
González-Alfonso, E., Fischer, J., Graciá-Carpio, J., et al. 2014b, A&A, 561, A27
González-Alfonso, E., Fischer, J., Sturm, E., et al. 2015, ApJ, 800, 69
González-Alfonso, E., Fischer, J., Spoon, H. W. W., et al. 2017, ApJ, 836, 11
González-Alfonso, E., Fischer, J., Bruderer, S., et al. 2018, ApJ, 857, 66
González-Alfonso, E., Smith, H. A., Fischer, J., & Cernicharo, J. 2004, ApJ, 613, 247
Greusard, D., Friedli, D., Wozniak, H., Martinet, L., & Martin, P. 2000, A&AS, 145, 425
Griffin, M. J., Abergel, A., Abreu, A., et al. 2010, A&A, 518, L3
Hao, C.-N., Kennicutt, R. C., Johnson, B. D., et al. 2011, ApJ, 741, 124
Heckman, T. M., Kauffmann, G., Brinchmann, J., et al. 2004, ApJ, 613, 109
Hunt, L. K., Combes, F., García-Burillo, S., et al. 2008, A&A, 482, 133
Indriolo, N., Neufeld, D. A., Seifahrt, A., & Richter, M. J. 2013, ApJ, 764, 188
Kamenetzky, J., Glenn, J., Maloney, P. R., et al. 2011, ApJ, 731, 83
Kennicutt, R. C., Jr 1998, ApJ, 498, 541
Kennicutt, R. C., & Evans, N. J. 2012, ARA&A, 50, 531
Kormendy, J. 1982, ApJ, 257, 75
Kormendy, J., & Ho, L. C. 2013, ARA&A, 51, 511
Kormendy, J., & Kennicutt, Jr., R. C. 2004, ARA&A, 42, 603
Lis, D. C., Neufeld, D. A., Phillips, T. G., Gerin, M., & Neri, R. 2011, ApJ, 738, L6
Liu, L., Weiß, A., Perez-Beaupuits, J. P., et al. 2017, ApJ, 846, 5
Maia, M. A. G., Machado, R. S., & Willmer, C. N. A. 2003, AJ, 126, 1750
Martín, S., Aladro, R., Martín-Pintado, J., & Mauersberger, R. 2010, A&A, 522, A62
Martín, S., Aalto, S., Sakamoto, K., et al. 2016, A&A, 590, A25
Mattila, K. 1986, A&A, 160, 157
McMullin, J. P., Waters, B., Schiebel, D., Young, W., & Golap, K. 2007, in Astronomical Data Analysis Software and Systems XVI, eds. R. A. Shaw, F. Hill, & D. J. Bell, ASp Conf. Ser., 376, 127
Mookerjea, B., Giesen, T., Stutzki, J., et al. 2010, A&A, 521, L13
Murphy, E. J., Condon, J. J., Schinnerer, E., et al. 2011, ApJ, 737, 67
Nagy, Z., Van der Tak, F. F. S., Ossenkopf, V., et al. 2013, A&A, 550, A96
Neufeld, D. A., Falgarone, E., Gerin, M., et al. 2012, A&A, 542, L6
Neufeld, D. A., Godard, B., Gerin, M., et al. 2015, A&A, 577, A49
Omont, A., Yang, C., Cox, P., et al. 2013, A&A, 551, A115
Pereira-Santaella, M., Alonso-Herrero, A., Rieke, G. H., et al. 2010a, ApJS, 188, 447
Pereira-Santaella, M., Diamond-Stanic, A. M., Alonso-Herrero, A., & Rieke, G. H. 2010b, ApJ, 725, 2270
Pereira-Santaella, M., Alonso-Herrero, A., Santos-Lleo, M., et al. 2011, A&A, 535, A93
Pereira-Santaella, M., Spinoglio, L., Busquet, G., et al. 2013, ApJ, 768, 55
Pereira-Santaella, M., Alonso-Herrero, A., Colina, L., et al. 2015, A&A, 577, A78
Pereira-Santaella, M., Colina, L., García-Burillo, S., et al. 2016, A&A, 594, A81
Pereira-Santaella, M., González-Alfonso, E., Usero, A., et al. 2017, A&A, 601, L3
Pereira-Santaella, M., Colina, L., García-Burillo, S., et al. 2020, A&A, 643, A89
Pfenniger, D., & Norman, C. 1990, ApJ, 363, 391
Pilbratt, G. L., Riedinger, J. R., Passvogel, T., et al. 2010, A&A, 518, L1
Piqueras López, J., Colina, L., Arribas, S., Pereira-Santaella, M., & Alonso-Herrero, A. 2016, A&A, 590, A67
Poglitsch, A., Waelkens, C., Geis, N., et al. 2010, A&A, 518, L2
Polehampton, E. T., Baluteau, J.-P., Swinyard, B. M., et al. 2007, MNRAS, 377, 1122
Rangwala, N., Maloney, P. R., Glenn, J., et al. 2011, ApJ, 743, 94
Regan, M. W., Vogel, S. N., & Teuben, P. J. 1997, ApJ, 482, L143
Rico-Villas, F., Martín-Pintado, J., González-Alfonso, E., Martín, S., & Rivilla, V. M. 2020, MNRAS, 491, 4573
Rodríguez-Zaurín, J., Arribas, S., Monreal-Ibero, A., et al. 2011, A&A, 527, A60
Roelfsema, P. R., Shibai, H., Armus, L., et al. 2018, PASA, 35, e030
Sakamoto, K., Aalto, S., Evans, A. S., Wiedner, M. C., & Wilner, D. J. 2010, ApJ, 725, L228
Sakamoto, K., Aalto, S., Costagliola, F., et al. 2013, ApJ, 764, 42
Scoville, N., Lee, N., Vanden Bout, P., et al. 2017, ApJ, 837, 150
Sheffer, Y., Rogers, M., Federman, S. R., et al. 2008, ApJ, 687, 1075
Shlosman, I., Frank, J., & Begelman, M. C. 1989, Nature, 338, 45
Snow, T. P., Destree, J. D., & Jensen, A. G. 2007, ApJ, 655, 285
Soltan, A. 1982, MNRAS, 200, 115
Spinoglio, L., Pereira-Santaella, M., Busquet, G., et al. 2012, ApJ, 758, 108
Tang, X. D., Henkel, C., Menten, K. M., et al. 2019, A&A, 629, A6
Thompson, T. A., Quataert, E., & Murray, N. 2005, ApJ, 630, 167
Tremaine, S., Gebhardt, K., Bender, R., et al. 2002, ApJ, 574, 740
Ward, J. S., Zmuidzinas, J., Harris, A. I., & Isaak, K. G. 2003, ApJ, 587, 171
Weiß, A., Requena-Torres, M. A., Güsten, R., et al. 2010, A&A, 521, L1
Welty, D. E., Federman, S. R., Gredel, R., Thorburn, J. A., & Lambert, D. L. 2006, ApJS, 165, 138
Wilson, T. L., & Rood, R. 1994, ARA&A, 32, 191
Yang, C., Gao, Y., Omont, A., et al. 2013, ApJ, 771, L24
Yang, C., Omont, A., Beelen, A., et al. 2016, A&A, 595, A80
Yang, C., González-Alfonso, E., Omont, A., et al. 2020, A&A, 634, L3
Younger, J. D., Hopkins, P. F., Cox, T. J., & Hernquist, L. 2008, ApJ, 686, 815

Appendix A: *Herschel*/PACS and SPIRE observations of ESO 320-G030 and models

We have applied our composite model for H_2O to all other molecular absorption features detected in the far-IR with *Herschel*/PACS. Models were generated for H_2O, $H_2^{18}O$, OH, ^{18}OH, OH^+, H_2O^+, H_3O^+, NH, NH_2, NH_3, CH, CH^+, $^{13}CH^+$, SH, HF, C_3, and H_2S, and the resulting modeled spectrum is overlaid with the spectra of all observed PACS wavelength ranges in Fig. A.1[4]. Model predictions at submm wavelengths are also compared with the *Herschel*/SPIRE spectrum of ESO 320-G030 in Fig. A.2.

Models for species other than H_2O have the intrinsic uncertainty of the contribution of each component to the line absorption or emission. We have adopted the following criteria: (i) Since the optically thin envelope generates little absorption in the H_2O lines, it is only included when needed, that is, for species that require it to obtain a reasonable fit in some lines. These are OH, OH^+, and NH_2. (ii) For the species $H_2^{18}O$ and ^{18}OH, we adopt a fixed column density ratio relative to the main isotopologues in the core and the disk. For the other species we started by assuming the same abundance in the core and the disk, but later relaxed this assumption for some species to obtain a better fit to the observed lines. (iii) In addition, we allowed for some flexibility in the value of τ_{100} for the disk and the envelope, relative to the fiducial model. In Table 2, the envelope has a fiducial $\tau_{100} = 0.22$, but both OH and OH^+ are better reproduced with $\tau_{100} = 0.34$. In addition, τ_{100} of the disk is allowed to vary between the fiducial value of 1.5 and 3. The increase in τ_{100} has the effect of enhancing the modeled molecular absorption at >130 μm. (*iv*) For most species (OH, ^{18}OH, OH^+, H_3O^+, NH, CH, CH^+, $^{13}CH^+$, C_3, and SH) an inflow velocity of 60 km s^{-1} was included in the disk model to match the position of the observed absorption features, which further indicates that the inflowing gas is still present at galactocentric distances of only ~40 pc. The column densities and abundances in the very saturated core component are obviously uncertain, and we rely mostly on the values in the disk for which uncertainties are expected to be better than 0.4 dex.

OH. All observed doublets at 65.2, 71.2, 79.2, 84.3, 119.3, and 163.2 μm are detected (see also Sect. 4.2). A very high OH abundance in the core is apparently required to nearly reproduce the OH 71 and 65 μm absorption, but it is significantly lower in the disk. The model overpredicts to some extent the absorption in the OH 119 μm doublet.

$H_2^{18}O$. Absorption lines are detected at 75.9, 109.4, and 139.6 μm, although the first two lines are close to the edge of the observed wavelength ranges. The lines are reproduced by assuming the same $N(H_2O)/N(H_2^{18}O) = 100-150$ ratio in the core and the disk. The resulting model reproduces rather well the $H_2^{18}O$ submm lines at 250, 264, 272, and 402 μm (Fig. A.2).

^{18}OH. The observed doublets at 65.7, 85, and 120 μm are nearly reproduced with $N(OH)/N(^{18}OH) = 100-150$, a value similar to that found for H_2O. The enhancement of ^{18}O in the nuclear region of ESO 320-G030 is higher than in the Galactic Center (~250, see Wilson & Rood 1994, and references therein), higher than in M 82 and NGC 253 (Martín et al. 2010), similar to the value in Arp 220 (González-Alfonso et al. 2012), and lower than in Mrk 231 (González-Alfonso et al. 2014b).

OH^+. The 3 absorption lines at 76.2−76.5 μm are primarily generated in the core, while the 152.3−153.1 and 158.4 μm lines at longer wavelengths are expected to be produced by the disk. To reproduce these features, a high OH^+ abundance of $\sim(0.6 - 1) \times 10^{-7}$ is required in both components, comparable to the value inferred in Mrk 231 (González-Alfonso et al. 2018). Additional contribution by the envelope with a similar OH^+ abundance is included to better match the strong absorption at 153 μm. By contrast, no far-IR OH^+ absorption is detected in the high spectral resolution (Fabry-Pérot) spectrum of Sgr B2 taken with the Infrared Space Observatory (ISO; Polehampton et al. 2007). Although the far-IR OH^+ absorption is prominent, the ground-state lines in the submm are hardly seen (Fig. A.2), which is consistent with the model.

H_2O^+. Absorption features are seen at 65.5 (blended with NH_2), 78.55, 143.3, 143.8 (blended with C_3), and 145.9−146.2 μm, although the latter features are shifted relative to the expected positions. Our model assumes the same abundance in both the core and the disk, 3×10^{-8}, and the 143.3 μm is somewhat overpredicted. Hence, a ratio $OH^+/H_2O^+ \sim 2-3$ is inferred. The model for H_2O^+ satisfactorily reproduces the submm lines at 400−420 μm.

H_3O^+. The clearest evidence of H_3O^+ absorption is found at the red edge of the NH_3 166 μm absorption, with hints of absorption also seen at 82.3 and 82.9 μm but no detected absorption at 69.55 μm. The latter constrains the H_3O^+ abundance to $\sim 3 \times 10^{-8}$, but the feature at 166 μm is not fully reproduced. It is possible that formation pumping enhances this absorption, as favored in Arp 220 (González-Alfonso et al. 2013). Results are consistent with $H_2O^+/H_3O^+ \sim 1$.

NH. Strong absorption features are detected at 76.6−76.9, 151.1, 151.5 (blended with C_3), 153.1 (blended with OH^+), and 153.4 μm, with additional hints of absorption at 153.7 μm. A high NH abundance of $\sim 5 \times 10^{-7}$ in both components is required to match the observed absorption. At submm wavelengths, the model predicts little absorption in the ground-state lines at 300, 308, and 317 μm. While this is consistent with the lack of absorption features at 308 and 317 μm, the absorption observed at 300 μm remains underpredicted.

NH_2. Absorption is detected at 65.6 (blended with H_2O^+), 78.4−78.6, and 130.2 μm, which we use to estimate the NH_2 column density. NH_2 also has strong lines in the submm at 207−208 μm (in absorption) and ~300−330 μm (in emission), which are reasonably reproduced by the model after adding an envelope contribution to the model (with a NH_2 abundance of 1.5×10^{-8}). The abundance of NH_2 in the core and disk components is about one order of magnitude lower than NH, in contrast with the abundance ratio in Sgr B2 where NH_2 is much more abundant than NH (Goicoechea et al. 2004). This suggests that there is an additional source of ionization in ESO 320-G030, probably due to cosmic rays.

NH_3. Absorption features are detected at 71.6, 83.4, 83.6−84.0, 84.5 (blended with OH), 165.7, and 170 μm, which are reproduced with a high NH_3 abundance of $\sim 10^{-6}$. The model also approximately accounts for the observed ground-state para-NH_3 absorption at 256.6 μm ($2_1^- - 1_1^+$). We then infer $NH_3/NH_2 \sim 20$, a ratio similar to the value in Sgr B2 (Goicoechea et al. 2004). The nitrogen chemistry in ESO 320-G030 appears to be the result of a combination of shock chemistry and high ionization rates.

CH. The doublet $N, J = 3, 7/2 \leftarrow 2, 5/2$ with $E_{lower} = 105$ K is detected at 118.4−118.7 μm. The model, with a CH abundance

[4] The $\lambda_{rest} = 63.0-63.4$ μm range has an Obs ID 1342212227; all other Obs ID are listed in Table 1.

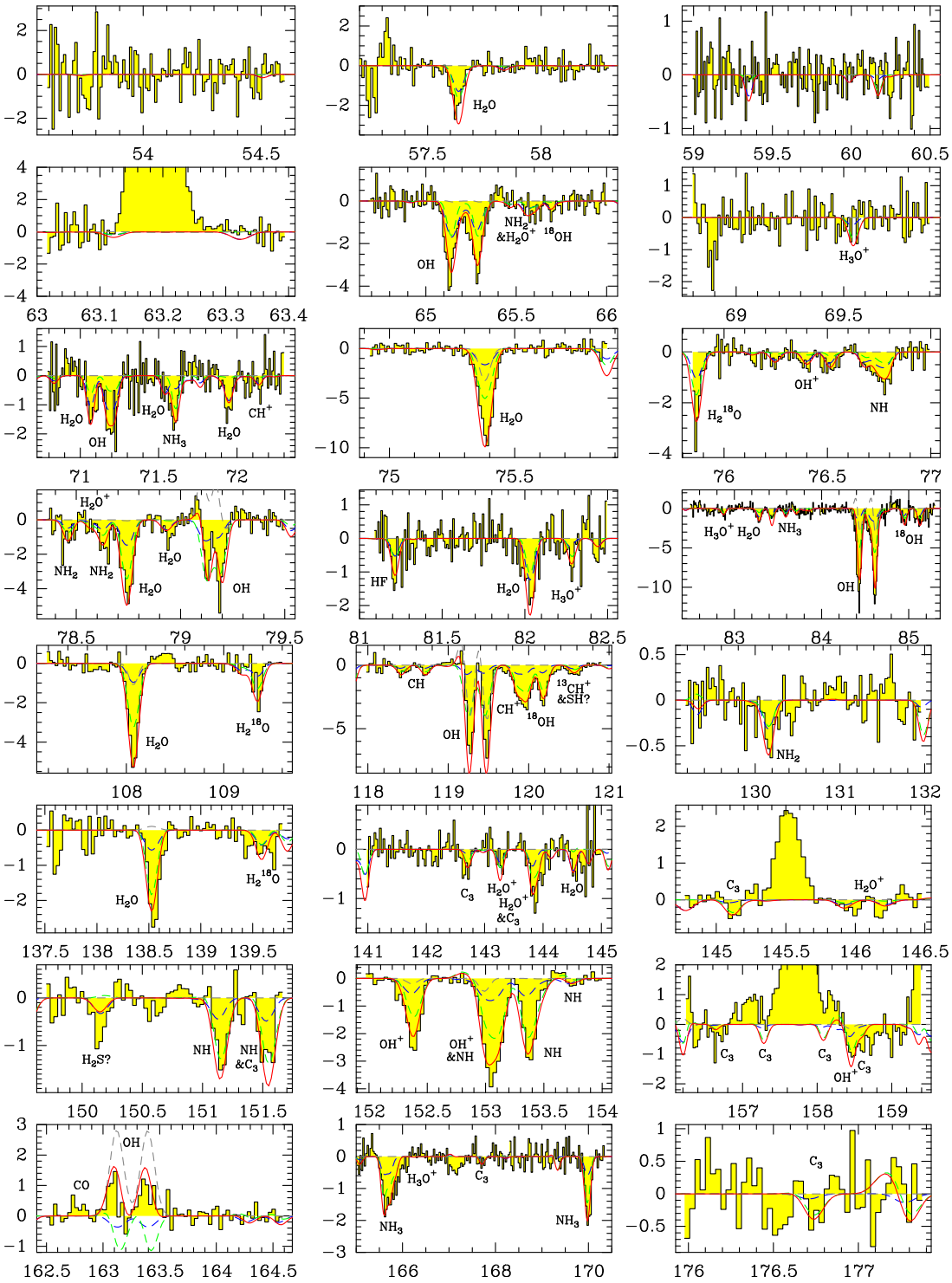

Fig. A.1. Overall model fit to all molecular features detected with *Herschel*/PACS in ESO 320-G030, including H_2O, $H_2^{18}O$, OH, ^{18}OH, OH^+, H_2O^+, H_3O^+, NH, NH_2, NH_3, CH, CH^+, HF, C_3, and H_2S (for this last species, see text). The contribution by the core, the nuclear disk, and the envelope is shown with dashed blue, green, and gray; red is total. The carriers of the modeled features (some of them undetected) are indicated. The abscissa indicates rest wavelength in μm, and the ordinate axis is the continuum-subtracted flux density in Jy.

of $\sim 5 \times 10^{-8}$, is consistent with the lack of detection of CH at 203–204 μm. Our derived abundance is a factor of $\approx$2.5 higher than the value derived in dark molecular clouds (Mattila 1986) and diffuse clouds (Sheffer et al. 2008). Formation of CH from CH^+, which is very abundant (see below), may be favored (Welty et al. 2006).

CH^+. Clear absorption is observed at 119.8 μm, adjacent to the redshift component of the ^{18}OH doublet at 120 μm. While this absorption is in principle attributable to both the CH^+ 3–2 line and to ^{17}OH ground-state absorption, the latter species is not expected to contribute significantly because the other component of the doublet at $\approx$119.62 μm is not detected (see

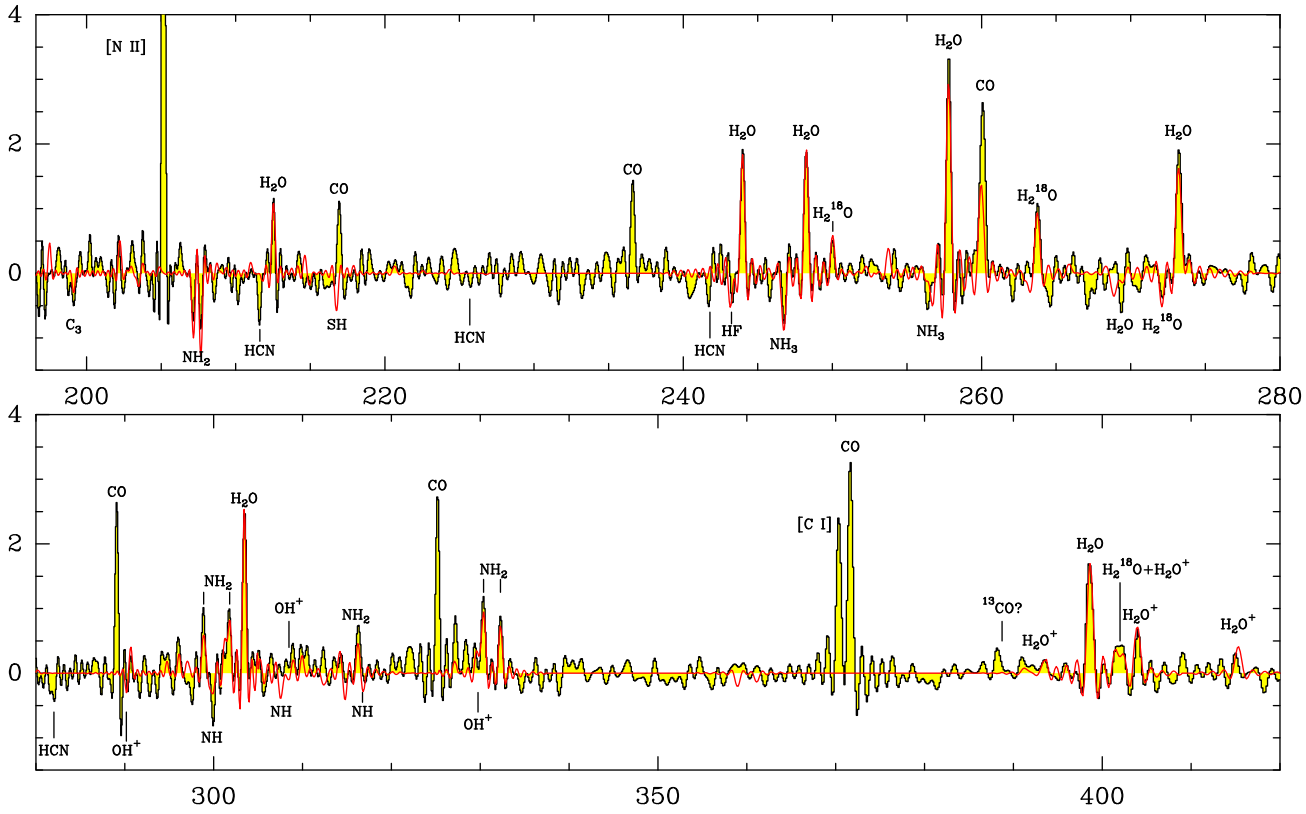

Fig. A.2. Comparison between the observed *Herschel*/SPIRE spectrum (up to 420 μm, filled histograms) observed in ESO 320-G030 and the predictions by the multispecies model (in red). The modeled spectrum has been convolved to the appropriate sinc function. The abscissa indicates rest wavelength in μm, and the ordinate axis is the continuum-subtracted flux density in Jy.

Table A.1. Column density ratios and abundances X of species Y included in the overall fit of the *Herschel*/PACS spectrum of ESO 320-G030.

	Core		Disk	
Species Y	$N(H_2O)/N(Y)$	X [a]	$N(H_2O)/N(Y)$	X [a]
H_2O	1	4×10^{-5}	1	1×10^{-5}
$H_2^{18}O$	100	4×10^{-7}	100	1×10^{-7}
OH	2	2×10^{-5}	1	5×10^{-6}
^{18}OH	100	2×10^{-7}	100	5×10^{-8}
OH^+	280	1×10^{-7}	140	6×10^{-8}
H_2O^+	1200	3×10^{-8}	350	3×10^{-8}
H_3O^+	1200	3×10^{-8}	350	3×10^{-8}
NH	75	5×10^{-7}	20	4×10^{-7}
NH_2	620	6×10^{-8}	175	7×10^{-8}
NH_3	38	1×10^{-6}	10	1×10^{-6}
CH	740	5×10^{-8}	210	4×10^{-8}
CH^+	180	2×10^{-7}	50	2×10^{-7}
$^{13}CH^+$	3600	1×10^{-8}	1050	1×10^{-8}
SH	1800	2×10^{-8}	520	2×10^{-8}
HF	1800	2×10^{-8}	520	2×10^{-8}
C_3	180	2×10^{-7}	30	3×10^{-7}

Notes. [a]Abundances X of species Y relative to H nuclei are estimated from the column density $N(Y)$ and the continuum optical depth at 100 μm ($N_H = 1.3\times10^{24}\,\tau_{100}$).

also Fischer et al. 2010). On the other hand, the CH^+ 5−4 line at 72.3 μm is not detected. To account for the CH^+ 119.8 μm absorption, a very high abundance of ~2×10^{-7} is required, which is consistent with the lack of detection of the ground-state line at 359 μm. A similarly high CH^+ abundance has been inferred by Nagy et al. (2013) toward the Orion Bar, but only within a narrow A_V-range where reaction of C^+ with vibrationally excited H_2 can overcome the high activation barrier of the formation reaction $C^+ + H_2 \rightarrow CH^+ + H_2$. The much higher implied column densities of CH^+ in the nucleus of ESO 320-G030 may indicate the additional combined effect of widespread dissipation of turbulence, shocks, and ionization by cosmic rays. A column density ratio $N(CH)/N(CH^+)$ ~ 0.7−2 is found in the Magellanic Clouds (Welty et al. 2006), while this ratio is ~0.25 in ESO 320-G030.

$^{13}CH^+$. A broad absorption feature is detected at 120.55 μm, which could be associated with either $^{13}CH^+$ 3−2 and/or to SH (see below). To check if it can be reproduced with only $^{13}CH^+$, a model with a fixed abundance ratio $^{13}CH^+/CH^+ = 0.05$ is used, appropriate for the central regions of starburst galaxies (Tang et al. 2019). The resulting modeled $^{13}CH^+$ 3−2 absorption accounts for approximately half of the observed 120.55 μm feature. It is possible that the $^{13}CH^+$ abundance in ESO 320-G030 is even higher than the adopted value, as in the very center of NGC 4945 (Tang et al. 2019).

SH. We have attempted to fill in the remaining 120.55 μm absorption by including a model for SH; the transition that may contribute to the observed absorption feature is $^2\Pi_{3/2}\ J = 9/2 \leftarrow 7/2$ ($E_{lower} \approx 160$ K). A constraint on the SH model is that it generates ground-state absorption at 217 μm, close to the CO 12−11 line. From the observed CO SLED, we expect little contamination by SH to CO 12−11, implying an upper limit to the SH

abundance of $\sim 2 \times 10^{-8}$. The 120.55 μm absorption is then still underpredicted. The quoted SH abundance is a factor of $\approx$1.5 higher than the highest SH abundance inferred in diffuse clouds (Neufeld et al. 2012, 2015), where SH only accounts for $\ll$1% of the gas-phase sulfur chemistry.

HF. A single far-IR feature is observed at 81.2 μm. We fix the HF abundance in both the core and the disk to the gas-phase fluorine abundance (Snow et al. 2007; Indriolo et al. 2013), and the observed HF 3−2 line is approximately reproduced. The model is also consistent with the apparent ground-state absorption at 243 μm. An undepleted chemistry is strongly suggested by these results.

C_3. Weak absorption features coincident with lines of the ν_2 band of C_3 are observed at 142.7, 143.8 (blended with H_2O^+), 145.1 and, imprinted on a wing emission in the [C II]157 μm line, at 157.3 and 158.1 μm. We thus favor the detection of C_3 in ESO 320-G030. The observed absorption lines are dominated by the disk, for which a very high abundance of several $\times 10^{-7}$ is required. For comparison, Cernicharo et al. (2000) and Mookerjea et al. (2010) infer an abundance of C_3 relative to H_2 in the galactic sources Sgr B2 and W31C of $(1-5) \times 10^{-8}$. The modeled spectrum predicts C_3 absorption features at 167.7 and 176.7 μm which are within the S/N of the observed spectra.

H_2S?. A relatively strong feature is detected at 150.15 μm, matching the expected position of the H_2S $4_{32}-3_{21}$ line ($E_{\rm lower} \approx$ 155 K). However, a similar or deeper absorption would be expected in the $3_{21}-2_{12}$ line at 144.78 μm, but it is not detected. The 151.15 μm feature is not detected in the (ISO) spectrum of Sgr B2 (Polehampton et al. 2007). The possible carrier of this absorption is considered unknown.

We have also indicated in Fig. A.2 the position of the HCN 12−11 to 16−15 lines (except the 13−12 line that is blended with CO at 260 μm). Apparent absorption features are detected at the wavelengths of the 12−11 (282 μm), 14−13 (242 μm), and 16−15 (212 μm) lines, but not at the position of the 15−14 transition at 226 μm. While this does not allow us to unambiguously associate the quoted spectral features to HCN, no alternative, reliable carriers have been found.

In summary, high enhancements in the abundance and column density of light hydrides are observed in the nuclear region of ESO 320-G030. In relation with Sgr B2, the prototypical high-mass star forming region in our galaxy with a nucleus optically thick in the far-IR, qualitative differences are seen in the absorption due to excited OH^+, CH^+, and also NH. These highly reactive species are widely observed in diffuse clouds through absorption from the ground-state level, but not in dense regions through absorption from rotational levels above the ground-state. Since the X-ray emission from the nucleus of ESO 320-G030 is weak (Pereira-Santaella et al. 2011), the source of molecular ionization is likely to be cosmic rays (see also the case of Mrk 231 in González-Alfonso et al. 2018). In addition, an undepleted chemistry (i.e., no grain mantles) generated by shocks and warm dust is strongly suggested.

Appendix B: 2D likelihood distributions of the free parameters

The posterior distribution of Eq. (3) is marginalized over to produce the 2D likelihood distributions of the free physical parameters, as shown in Fig. B.1. This enables an evaluation of the degeneracies among these parameters.

We find two main degeneracies: First, τ_{100} is degenerate with $N_{\rm H2O}$ in the core component. The extinction in this component is important even in the submm, so that an increase in τ_{100} reduces the width of the external shell responsible for the line absorption. As a consequence, the required H_2O column density increases to maintain the same value in the photosphere that can be traced. Second, the opposite effect is to some extent found in the envelope, where an increase in τ_{100} is accompanied by a decrease in $N_{\rm H2O}$. In this component, extinction by dust is negligible, and any increase in τ_{100} involves a stronger radiation field that is responsible for the H_2O excitation, thereby reducing to some extent the value $N_{\rm H2O}$ required to explain the observed line fluxes. Nevertheless, the values of τ_{100} and $N_{\rm H2O}$ in the envelope are still well constrained by the data.

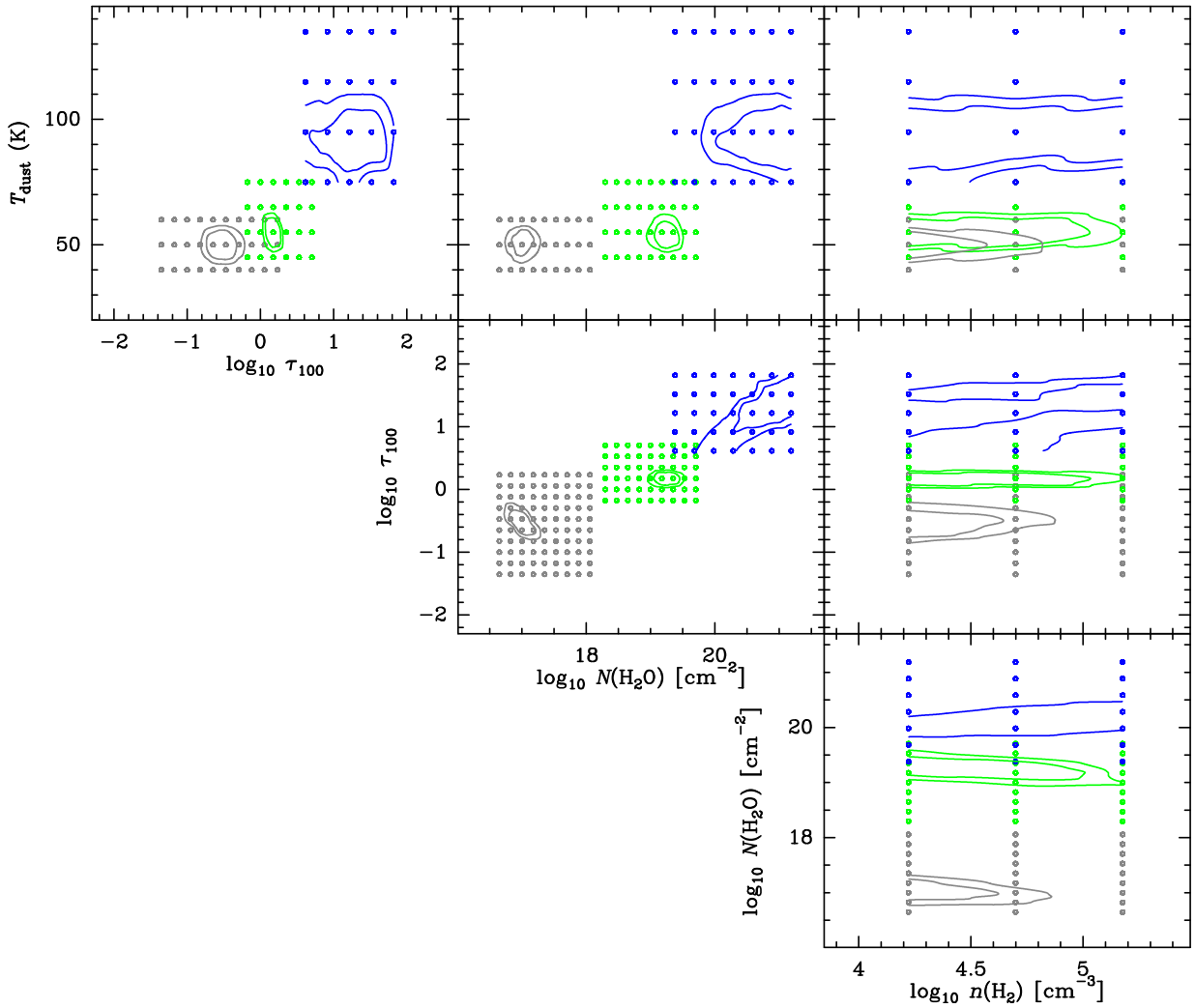

Fig. B.1. 2D marginalized posterior distributions of the free physical parameters of each component ($T_{\rm dust}$, τ_{100}, $N_{\rm H2O}$, $n_{\rm H2}$) included in our fits to the H_2O fluxes and continuum flux densities (Sect. 3.1.5). Each panel displays contours at 25% and 50% of the peak likelihood in the parameter-parameter space for each of the three components. Blue, green, and gray colors correspond to the core, the nuclear disk, and the envelope, respectively.